MODELING AND ANALYSIS OF HIGH FREQUENCY NOISE

IN BICMOS TRANSISTORS

by

Peng Cheng

APPROVED BY SUPERVISORY COMMITTEE:

_____

Dr. Rashaunda M. Henderson, Chair

_____

Dr. Hisashi Shichijo, Co-Chair

_____

Dr. Kenneth K. O

_____

Dr. William Frensley

MODELING AND ANALYSIS OF HIGH FREQUENCY NOISE IN BICMOS TRANSISTORS

by

Peng Cheng, BS, MS

DISSERTATION

Presented to the Faculty of

The University of Texas at Dallas

in Partial Fulfillment

of the Requirements

for the Degree of

DOCTOR OF PHILOSOPHY IN

ELECTRICAL ENGINEERING

THE UNIVERSITY OF TEXAS AT DALLAS

August 2019

ACKNOWLEDGMENTS

First of all, my sincere gratitude goes to Dr. Hisashi Shichijo and Dr. Rashaunda Henderson, my advisors, who have given me important advising in my academic research and support in my career. The guidance from them is significant and useful and has helped me a lot during my PhD study. I appreciate their understanding and support. I would also like to thank Dr. Kenneth K. O for the opportunity to work as a group member of Texas Analog Center of Excellence (TxACE). I am very grateful for learning the knowledges of most advanced analog and radio frequency circuit design, device physics and signal processing here.

I would also like to thank Dr. Kenneth K. O and Dr. William Frensley for their precious time as my PhD academic committee members and the valuable suggestions for my research. I appreciate their valuable comments and guidance on my PhD proposal.

Additionally, I would like to thank the colleagues and friends in TxACE. I would also like to acknowledge the faculty and staff in the Department of Electrical Engineering.

Finally, I would like to thank my parents and family, who support me and love me. They encouraged me through all the tough times in my research and personal life.

April 2019

MODELING AND ANALYSIS OF HIGH FREQUENCY NOISE

IN BICMOS TRANSISTORS

Peng Cheng, PhD
The University of Texas at Dallas, 2019

Supervising Professor: Rashaunda M. Henderson, Chair
Hisashi Shichijo, Co-Chair

The importance of high frequency noise performance is increasing in advanced bipolar and complementary metal-oxide semiconductor (BiCMOS) technologies because of the high demands of radio frequency (RF) and mixed-signal integrated circuits used in the 5G communication, automatic-driving sensors and internet of things (IOT) applications. While the characterization and modeling of high frequency noise of BiCMOS transistors have been a topic for many years, some important issues have not been clarified. For example, the noise correlation is not well predicted for bipolar devices, the excess noise factor is not well understood for MOSFET devices and the temperature dependence of high frequency noise in BiCMOS devices is not well studied. Focused on these issues, this research establishes the approach to extract the noise transit time from the high current compact model (HICUM), demonstrates an efficient methodology for high frequency noise prediction for silicon-germanium heterojunction bipolar transistors (SiGe HBTs) and validates the prediction methodology over size, bias and temperature.

One of the issues of high frequency noise modeling of bipolar transistors is the noise correlation effect. This research explores the physical origin of high frequency noise correlation, studies the

noise model of SiGe HBTs and creates an approach to extract the noise transit time from the HICUM compact model. The extracted noise transit time is validated by the tuner-based noise measurement results of sample SiGe HBTs by comparing the four noise parameters between the calculated and measured data over transistor size, bias and temperature. The results show that the noise transit time can be independent of frequency but dependent on bias and temperature. Furthermore, a complete high frequency noise prediction system is established.

Based on the extraction methodology of the noise transit time from the HICUM model, this dissertation demonstrates a low-cost and time-friendly methodology to predict the full high frequency noise properties of the bipolar devices directly from the S-parameter measurement, DC measurement and the parameters from the HICUM model without the tuner-based noise measurement. Compared with the conventional tuner-based noise measurement, this methodology can save the measurement time as well as achieve a good accuracy.

For MOSFET devices, the importance of excess noise factor is increasing with the transistor size scaling down to sub-100nm for high frequency noise modeling, but it has not been well studied so far. This research analyzes the excess noise factor based on the device physics and characterization results, investigates the noise sources contribution and models the high frequency noise based on Y-parameter methodology.

TABLE OF CONTENTS

LIST OF FIGURES

LIST OF TABLES

CHAPTER 1

INTRODUCTION

In order to satisfy the communication and social connection demands for people's daily lives, wireless communication techniques have rapidly developed in recent decades. State-of-the-art research has concentrated on many RF and mixed-signal integrated circuit applications, such as 5G communication, internet of things (IoT) and auto-driving radar sensors. As the circuit designs increasingly move into the RF and millimeter-wave frequency range, the silicon-germanium heterojunction bipolar transistor (SiGe HBT) has been developed with high cut-off frequency (f_T/f_{max}), good noise performance and excellent integration ability with Si CMOS for system-on-a-chip solutions. In the meantime, with the development of nanoscale MOSFET technology, the f_T/f_{max} are also increasing rapidly, which can be available for RF and millimeter-wave circuit designs with the benefits of high-level integration capability. In conclusion, advanced SiGe HBT and CMOS technologies are both widely used in RF and millimeter-wave circuit designs. Therefore, the characterization and modeling of scaled SiGe bipolar and CMOS (BiCMOS) technologies are becoming significantly important.

1.1 Motivation

SiGe BiCMOS technology is increasingly preferred in RF and millimeter-wave circuit designs with its good system-on-a-chip flexibility and cost advantage for large volume production. For RFIC applications, RF noise performance is one of the critical design characteristics, which is important in wireless commutation transceivers. For example, in a low noise amplifier (LNA), the noise figure of the first stage transistor in the circuit affects the total noise figure of the system.

Therefore, the LNA should be designed with lower noise and higher gain. As another example, in an analog digital convertor (ADC), the signal to noise ratio (SNR) will be dominated by the transistor noise level. In conclusion, the noise performance of the transistors affects the performance of the wireless circuits and it needs to be well characterized and modeled to meet the requirements of RFIC designs.

The most common high frequency noise characterization method is tuner-based source-pull noise measurement. But this kind of noise measurement is usually time consuming and the tuner itself is expensive. Therefore, this measurement method does not have the capability for handling a large amount of measurement demands especially in the process technology development stage. Therefore, it is meaningful to find an efficient noise prediction methodology with a comparable or better accuracy.

Compact models are used to predict the high frequency noise properties of the BiCMOS devices. Unfortunately, the available compact models of bipolar devices cannot reasonably predict the noise properties over the size, bias and temperature because of the deficiency in the calculation of high frequency noise correlation. Therefore, this dissertation investigates the noise correlation and describes a noise prediction methodology based on HICUM model and Y-parameter data for SiGe HBTs. At the same time, the high frequency noise is not well modeled for MOSFET devices especially for short-channel analog MOSFET devices because of the uncertainty in the excess noise factor. Therefore, our research is valuable for clarifying the noise correlation effect for bipolar transistors and analyzing the excess noise factor for MOSFET devices to improve the compact noise models.

In conclusion, this research is proposed for meeting the demand of time-friendly and accurate high frequency noise prediction of advanced BiCMOS devices. At the same time, the research gives a better cognition of the high frequency noise modeling of BiCMOS devices, based on the noise analysis over the size, bias and temperature. This research will benefit the areas of process development, device modeling and characterization and circuit design.

1.2 Overview

The following chapters provide the detailed methodology of high frequency noise prediction and parameter extraction of BiCMOS devices. To demonstrate this methodology, this dissertation includes the information about the RF noise measurement system, RF noise de-embedding techniques and RF noise modeling with compact models. The experimental results are indicated in the dissertation to validate the models.

Chapter 2 gives an introduction of the background knowledge and fundamental concepts about the high frequency noise in BiCMOS transistors, discusses multiple noise sources and the derivation of four noise parameters.

Chapter 3 introduces the on-wafer noise measurement system and the de-embedding techniques for the characterization of high frequency noise of on-wafer devices.

Chapter 4 discusses the noise correlation effect and the extraction of noise transit time of SiGe HBTs based on HICUM compact model. At the same time, the validation of Y-parameter noise calculation methodology and the noise correlation model based on the experimental results are discussed.

Chapter 5 discusses the RF noise calculation and modeling of MOSFET transistors. This chapter also explains the analysis of excess noise factor over the temperature and transistor size based on the experimental results.

Chapter 6 concludes with a summary of the research and future works.

CHAPTER 2

FUNDAMENTALS OF NOISE

Noise is generated by many sources in the world including artificial and natural sources. In the electrical area, noise always comes with the signal and can be a challenge for the RFIC designers. For example, the received signal of a cell phone can be interfered by the background white noise as shown in Fig. 2.1. Besides this, other noise sources come from the device itself, and these noise sources limit the performance of electronics, by affecting the sensitivity and robustness of the system. These noise sources need to be well characterized.

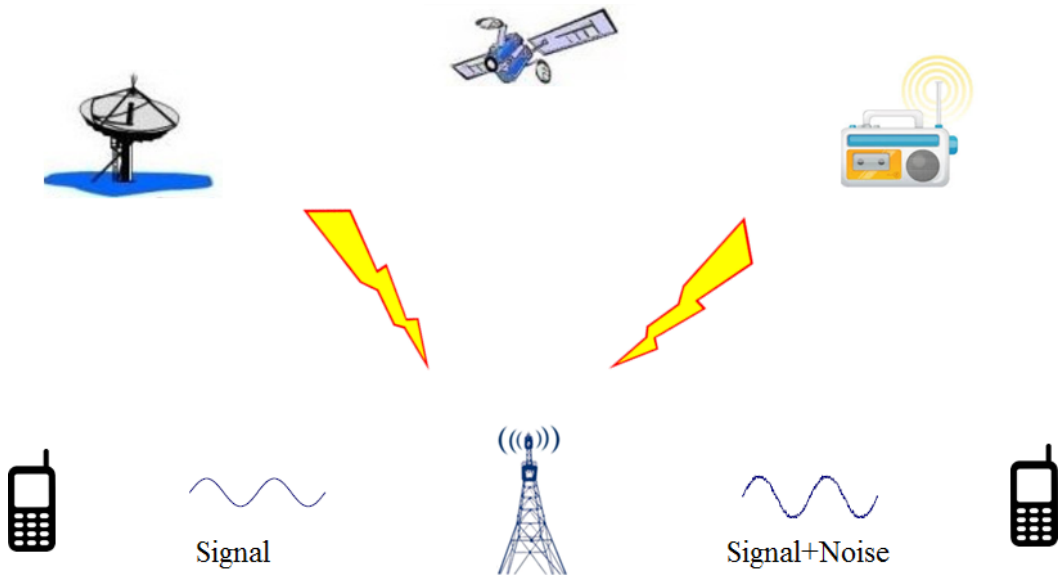

Figure 2.1. Noise sources. [1]

This dissertation will mainly discuss the noise at high frequency such as thermal and shot noise, which are the dominating noise components in the RFIC frequency range.

2.1 Thermal Noise

Thermal noise or Nyquist noise is the electronic noise generated by the thermal agitation of the charge carriers (usually the electrons) inside an electrical conductor in thermal equilibrium with a random walk Brownian motion, which happens regardless of any applied voltage. Johnson discovered and verified that the power density of the thermal noise is nearly constant in the frequency spectrum [2] and its value is only dependent on the electrical resistance and temperature. The internal noise voltage source or current source is described by the Nyquist equation [3]

$$\langle v_n^2 \rangle = 4kTR\Delta f \tag{2.1}$$

$$\langle i_n^2 \rangle = \frac{4kT\Delta f}{R}, \tag{2.2}$$

where k is the Boltzmann's constant, T is the absolute temperature, R is the resistance and Δf is the bandwidth. The thermal noise is white like, which means it has a flat spectrum over the frequencies with a zero-average amplitude in time. However, the power spectral density of thermal noise is not zero. It can be described as a voltage or current source,

$$S_{nv} = 4kTR \tag{2.3}$$

$$S_{ni} = \frac{4kT}{R}. \tag{2.4}$$

These spectral densities of the thermal noise are proven to be constant up to 1 THz. Therefore, in the frequency range we are interested in (2 GHz to 18 GHz) the thermal noise can be determined from measuring the temperature and resistance. Thermal noise is associated with every physical resistor and it is the most basic component of the noise sources of electronic devices.

2.2 Shot Noise

Shot noise is associated with a Poisson stream of electricity and the individual carrier injection through the pn junction [4]. The transition of the charges needs to overcome a potential barrier. Each of the events causes a random current pulse to occur at the external terminal. The power spectrum density of this random process is given by [4]

$$S_{nsh} = 2qI\ , \tag{2.5}$$

where q is the electron charge and I is the junction current. The noise power spectrum density of the shot noise is temperature independent and its value is only proportional to the dc current passing through the junction.

Shot noise is usually considered as a current source connected in parallel to the small signal junction resistance. It is usually the dominant component of the bipolar noise sources at high frequency.

2.3 Flicker Noise

Flicker noise or low-frequency noise is ubiquitous in almost every electronic device. It is the dominant noise in the low frequency range and its power spectral density is proportional to $1/f$, so it is also called $1/f$ noise. In some theories, the flicker noise source is attributed to the fluctuation in the carrier mobility. However, a unified theory for the mechanisms of $1/f$ noise is still an open topic. $1/f$ noise exists in the low frequency range compared with the RF noise that is discussed in this dissertation. Two major models are used to describe the $1/f$ noise: the surface model developed by McWhorter [5] and the bulk model developed by Hooge [6]. The resulting noise spectral density function of McWhorter is given by

$$S_{1/f} \propto (\overline{\Delta N})^2 \int_{\tau_1}^{\tau_2} \frac{1}{\tau} \frac{4\tau}{1+\omega\tau^2} d\tau = (\overline{\Delta N})^2 \cdot \frac{1}{f} \qquad \left(for\ \frac{1}{\tau_2} \ll \omega \ll \frac{1}{\tau_1} \right), \tag{2.6}$$

where N is the number of electrons and τ is the trapping time constant. The McWhorter's model is usually used for the MOSFET modeling.

For BJTs, the Hooge's bulk model is more appropriate. The noise spectral density function is given by

$$S_{1/f} = \frac{\propto_H \cdot I^{\propto}}{f^{\gamma} \cdot N}, \tag{2.7}$$

where $\propto_H = 2 \times 10^{-3}$ is the Hooge constant, $\propto$ and γ are material constants and N is the number of carriers. Since the flicker noise is proportional to $1/f$, the power density becomes negotiable compared with thermal noise and shot noise beyond the corner frequency of approximately 100 KHz for bipolar and 100 MHz to 1 GHz for MOSFET devices as shown in Fig. 2.2. Therefore, in this dissertation, the high frequency noise modeling will only include the thermal noise and shot noise for both bipolar and MOSFET devices.

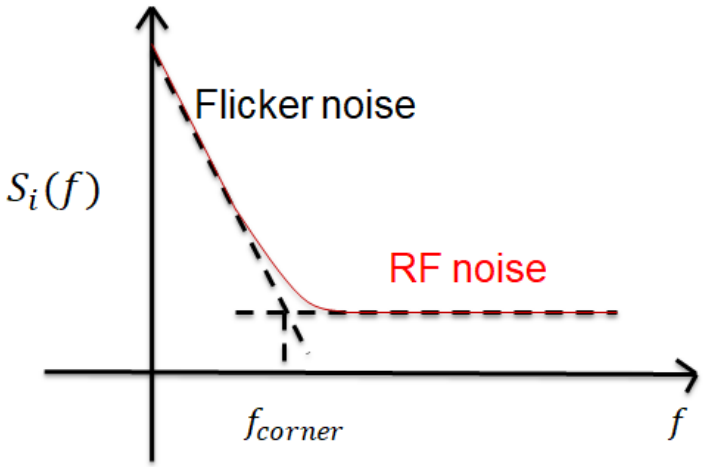

Figure 2.2. Transistor noise power spectral density.

2.4 Noise Figure

Noise figure (NF) or noise factor (F) is an important parameter to describe the noise performance of the electronic devices. This parameter is defined by the signal-to-noise power ratio (SNR) between the input and output of a network [7]

$$F \triangleq \frac{(SNR)_{in}}{(SNR)_{out}}, \tag{2.8}$$

where the ambient temperature is $T_0 = 290\ K$.

Modern usage of noise figure (NF) is usually in dB format which is convenient in RF engineering and is described by

$$NF = 10 \cdot \log(F)\,. \tag{2.9}$$

2.5 Four Noise Parameters

The noise factor of an electronic device is not only determined by the noise sources inside of the device but also determined by the admittance of the source driving it. The noise behavior of the transistor can be described by the well-known four noise parameters [8]

$$F = F_{min} + \frac{R_n}{G_s} \cdot \left|Y_s - Y_{opt}\right|^2, \tag{2.10}$$

where Y_s ($Y_s = G_s + jB_s$) is the source admittance, Y_{opt} is the optimum admittance point that gives the minimum noise factor F_{min}, and R_n is the equivalent noise resistance which indicates how fast the noise will increase as Y_s deviates from the optimum admittance point.

Fig. 2.3 shows examples of the 2D and 3D noise figure plots of a sample SiGe HBT transistor. To do this kind of measurement a tuner is needed at the input of the device under test

(DUT) to sweep the input impedance for each of the frequency point. Therefore, using the tuner-based system to measure the noise is time-consuming especially for a wide frequency range.

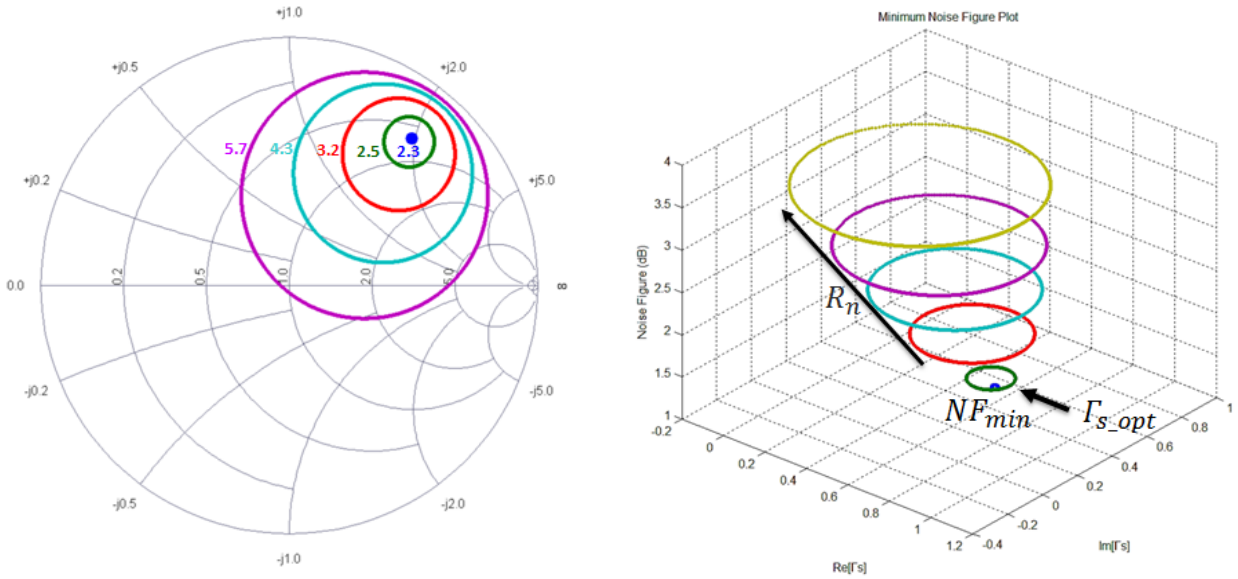

Figure 2.3. 2D and 3D plots of the noise figure dependent on source reflection coefficient Γ_s.

2.6 Two-port Noise Calculation

The two-port network representation simplifies the circuit calculation by putting the complex circuits inside a black box. This theory can be used for analyzing the high frequency noise of the electronic devices. As shown in Fig. 2.4, the two-port theory provides a thinking perspective that the noisy two-port network can be represented by a noise-free two-port block with an equivalent input noise voltage source v_n and a noise current source i_n. Then, the Y-parameters can be a useful tool to transform the modeled internal noise sources to the input of the noise-free block. In this section, the derivation of four noise parameters based on the two-port theory and Y-

parameters will be discussed and the details for noise calculation methodology of SiGe HBTs and MOSFETs with actual noise sources will be discussed in Chapters 4 and 5.

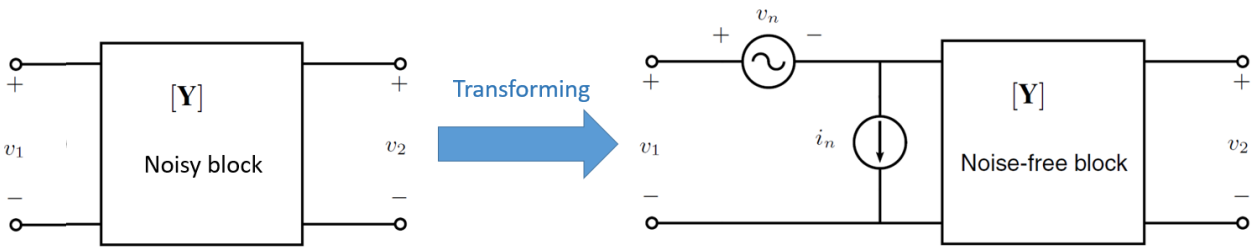

Figure 2.4. Representation transforming of a linear noisy 2-port network [9].

To calculate the noise factor, the network is connected with a source admittance Y_s and a noise current source i_s. The source connected network is shown as Fig. 2.5 and the noise calculation procedure is followed [8].

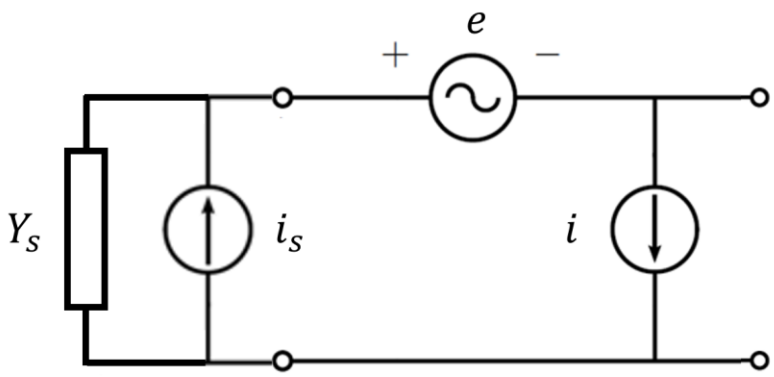

Figure 2.5. Network for noise calculation [8].

Then the mean-square of the total short-circuit noise current at the output can be obtained by

$$\overline{\imath_s^2} + \overline{|\imath + Y_s e|^2} = \overline{\imath_s^2} + \overline{\imath^2} + |Y_s|^2\overline{e^2} + Y_s^*\overline{\imath e^*} + Y_s\overline{\imath^* e}\,. \tag{2.11}$$

Based on the noise factor definition, the noise factor can be written as

$$F = 1 + \frac{\overline{|\imath + Y_s e|^2}}{\overline{\imath_s^2}}. \tag{2.12}$$

In the meantime, a mean-square current fluctuation of the source termination can be given in the unit of A^2/Hz and the quantity can be given by

$$\langle i_s^2 \rangle = 4kTG_s\Delta f\ , \tag{2.13}$$

where G_s is the source conductance.

To simplify the noise factor equation, we can split the noise current into two parts: one is correlated with the voltage source and the other is uncorrelated with the voltage source. The uncorrelated current is defined as i_u and the correlated one is defined as $i - i_u$

$$\overline{e\imath_u{}^*} = 0 \tag{2.14}$$

$$\overline{(\imath - \imath_u)\imath_u{}^*} = 0 \tag{2.15}$$

$$\overline{\imath - \imath_u} = Y_{cor}e\ , \tag{2.16}$$

where Y_{cor} ($Y_{cor} = G_{cor} + jB_{cor}$) is the correlation admittance.

Then the cross-product $\overline{e\imath^*}$ is obtained by

$$\overline{e(\imath - \imath_u)^*} = Y_{cor}^*\overline{e^2}\ . \tag{2.17}$$

The mean-square voltage fluctuation of e can be given in the unit of $volt^2/Hz$ and the quantity can be given using the Nyquist equation by

$$\overline{e^2} = 4kTR_n\Delta f\ , \tag{2.18}$$

where R_n is the equivalent noise resistance.

In the meantime, the uncorrelated current noise source can be given by

$$\overline{\imath_u{}^2} = 4kTG_u\Delta f. \tag{2.19}$$

The total noise current is obtained by

$$\overline{\iota^2} = \overline{|\iota - \iota_u|^2} + \overline{\iota_u{}^2} = 4kT[|Y_{cor}|^2 R_n + G_u]\Delta f \,. \tag{2.20}$$

Therefore, the noise factor equation can be written as

$$F = 1 + \frac{G_u}{G_s} + \frac{R_n}{G_s}[(G_s + G_{cor})^2 + (B_s + B_{cor})^2] \,. \tag{2.21}$$

This noise factor has a minimum value F_{min} at an optimum source admittance $Y_s = Y_{opt}$ ($Y_{opt} = G_{opt} + jB_{opt}$), where

$$G_{opt} = \sqrt{\frac{G_u + R_n G_{cor}{}^2}{R_n}} \tag{2.22}$$

$$B_{opt} = -B_{cor} \tag{2.23}$$

and the minimum noise factor is

$$F_{min} = 1 + 2R_n \left(G_{cor} + G_{opt}\right) . \tag{2.24}$$

Then the noise factor can be written as

$$F = F_{min} + \frac{R_n}{G_s}\left[\left(G_s - G_{opt}\right)^2 + \left(B_s - B_{opt}\right)^2\right], \tag{2.25}$$

where the four noise parameters are defined.

Based on the knowledge above, we can analyse the two-port equivalent circuits shown in Fig. 2.4. The chain matrix C_A is represented by the equivalent input noise sources [10], and is useful for the analysis of cascaded networks

$$C_A = \begin{bmatrix} C^*_{v_n v_n^*} & C^*_{v_n i_n^*} \\ C^*_{v_n^* i_n} & C^*_{i_n i_n^*} \end{bmatrix}. \tag{2.26}$$

Noise sources are described as power spectral densities, which are defined as the Fourier transform of their auto- and cross-correlation functions [10]

$$\overline{s_i s_j{}^*} = 2\Delta f C^*_{s_i s_j^*} \qquad (i,j = 1,2)\,. \tag{2.27}$$

Based on equations (2.23) and (2.24), Y_{cor} can be written by F_{min} , R_n and Y_{opt} as

$$Y_{cor} = \frac{F_{min} - 1}{2R_n} - Y_{opt}\,. \tag{2.28}$$

Then the chain matrix elements can be solved as

$$C^*_{v_n v_n^*} = \frac{1}{2\Delta f} \cdot \langle v_n^2 \rangle = 2kT \cdot R_n \tag{2.29}$$

$$C^*_{i_n i_n^*} = \frac{1}{2\Delta f} \cdot \langle i_n^2 \rangle = 2kT \cdot R_n \left|Y_{opt}\right|^2 \tag{2.30}$$

$$C^*_{v_n^* i_n} = \frac{1}{2\Delta f} \cdot Y_{cor} \langle v_n^2 \rangle = 2kT \cdot Y_{cor} R_n = \; 2kT \cdot \left(\frac{F_{min} - 1}{2} - R_n Y_{opt}\right). \tag{2.31}$$

Then the *ABCD* representation of the correlation matrix is given by

$$C_A = \; 2kT \begin{bmatrix} R_n & \dfrac{F_{min} - 1}{2} - R_n Y_{opt}^* \\ \dfrac{F_{min} - 1}{2} - R_n Y_{opt} & R_n \left|Y_{opt}\right|^2 \end{bmatrix}. \tag{2.32}$$

The four noise parameters can then be obtained as [8]

$$R_n = \frac{\langle v_n^2 \rangle}{4kT} \tag{2.33}$$

$$Y_{opt} = \sqrt{\frac{\langle i_n^2 \rangle}{\langle v_n^2 \rangle} - \left[\Im\left(\frac{\langle v_n i_n^* \rangle}{\langle v_n^2 \rangle}\right)\right]^2} + j\Im\left(\frac{\langle v_n i_n^* \rangle}{\langle v_n^2 \rangle}\right) \tag{2.34}$$

$$F_{min} = 1 + \frac{\langle v_n i_n^* \rangle + \langle v_n^2 \rangle Y_{opt}^*}{2kT}\,, \tag{2.35}$$

where k is the Boltzmann constant, T is the absolute ambient temperature and $Y_{opt} = G_{opt} + jB_{opt}$.

2.7 Conclusion

This chapter introduced the fundamentals of noise theory and the internal noise source models for electronic devices. This chapter also discussed the definition of the noise figure and four noise parameters, which are the important parameters to represent the noise performance of a transistor. In the end, this chapter indicated the two-port theory and the Y-parameters method for calculating the four noise parameters. Based on the knowledges in this chapter, Chapter 4 and Chapter 5 will introduce the methodologies for high frequency noise calculation for SiGe HBT and MOSFET devices.

CHAPTER 3

HIGH FREQUENCY NOISE MEASUREMENT

To model the high frequency noise and validate the model accuracy of BiCMOS transistors generally requires measuring the transistor's S-parameters and four noise parameters over bias, size and temperature. Some of the model parameters, such as the dc current and zero-bias output conductance (g_{ds0}), are measured and extracted from the *I-V* data. In this research, we are interested in the high frequency noise performance of transistors. Therefore, the noise measurement frequency range is chosen to be from 2 GHz to 18 GHz.

3.1 Tuner-based Noise Measurement System

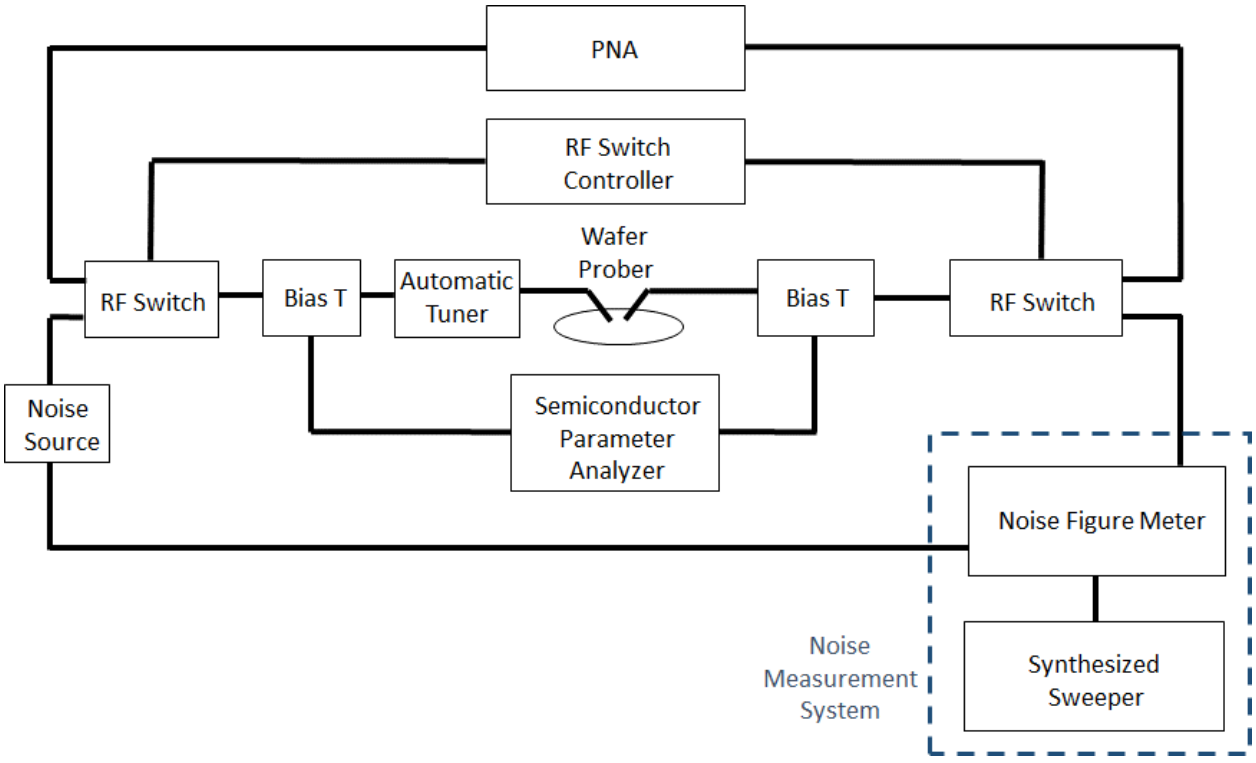

Figure 3.1. Tuner-based on-wafer noise measurement system block diagram.

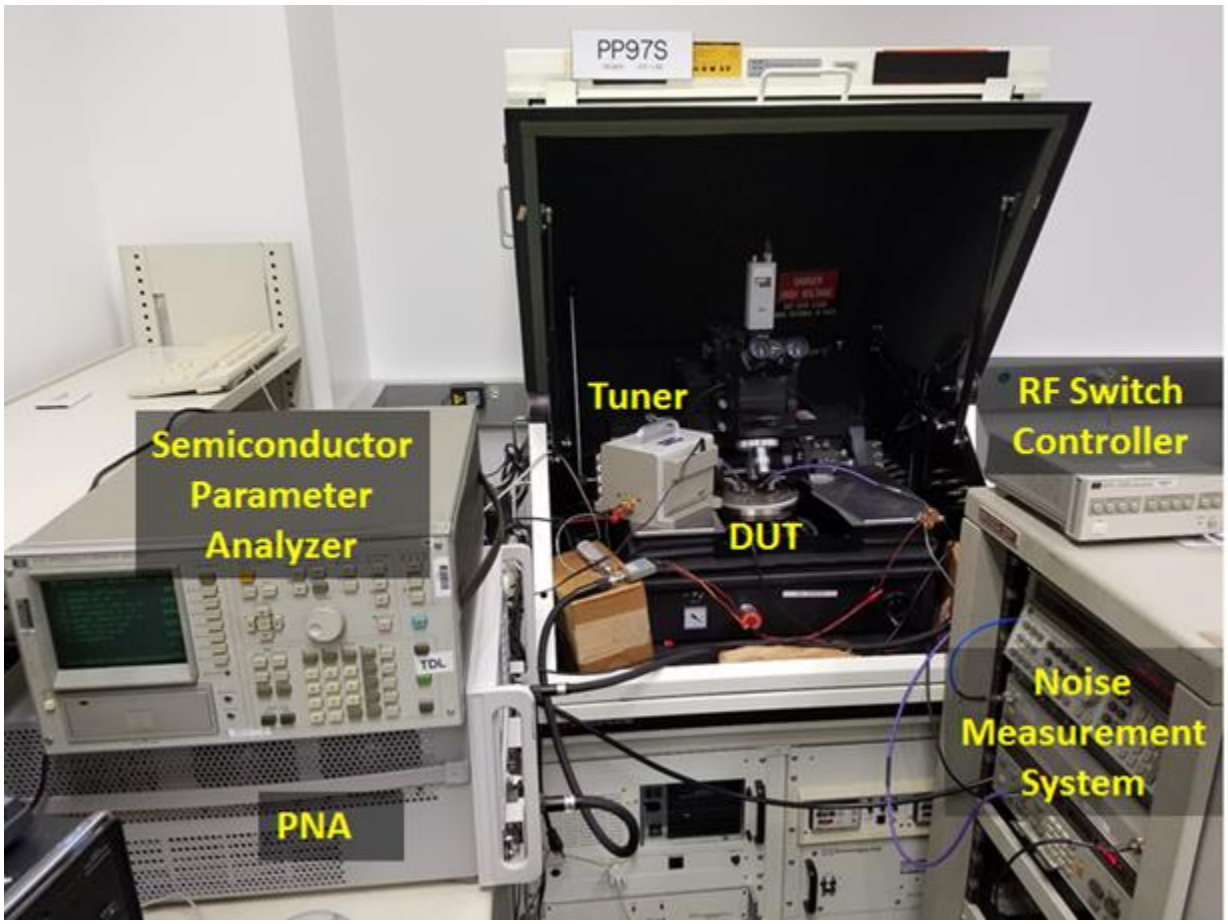

Figure 3.2. Tuner-based on-wafer noise measurement system.

To fully characterize the noise parameters of a device, a tuner is needed at the input to sweep the input admittance. Fig. 3.1 and Fig. 3.2 show how to realize the tuner-based on-wafer noise measurement system. Fig. 3.1 is a block diagram of the tuner-based measurement system, which can measure the device full noise paramerters: F_{min}, R_n and Y_{opt} over the frequency of interest. The automated tuner is used to vary the source admittance. RF switches are used to change the configuration between the S-parameter measurement by PNA (E8361C) and the noise measurement by the noise source and the noise figure meter. The semiconductor parameter analyzer is used to provide appropriate bias to the device.

Fig. 3.2 is a photograph of the actual measurement system implemented at The University of Texas at Dallas. This system includes on-wafer probes with a temperature chuck which can vary the device temperature from 25 °C to 150 °C.

The controller software of the noise measurement system is ATS (Automated Tuner System) from Maury Microwave Corporation.

3.2 De-embedding Techniques

To eliminate the surrounding parasitics on the wafer, de-embedding techniques should be applied on the measured S-parameter data as well as the measured four noise parameters. In this chapter, we will introduce the de-embedding techniques by OPEN&SHORT dummy structures, which are necessary for calculating the noise performance of intrinsic devices.

3.2.1 De-embedding of S-parameters

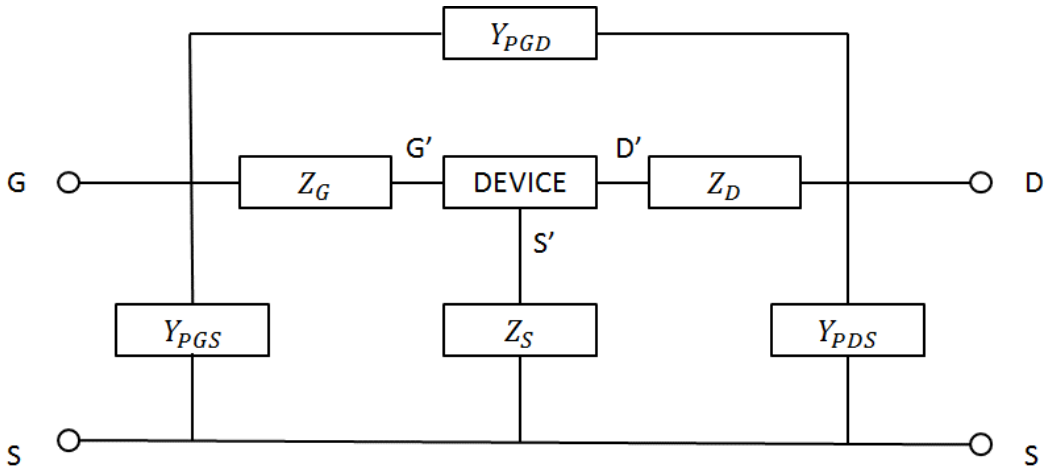

Figure 3.3. Equivalent pads circuit diagram [11].

The S-parameter measurement is performed on the DUT and OPEN&SHORT dummy structures. With the obtained S-parameter results [S_{DUT}], [S_{OPEN}] and [S_{SHORT}], the surrounding parasitics are removed based on the procedures described in [11] as follows.

1. Convert [S_{DUT}], [S_{OPEN}] and [S_{SHORT}] to [Y_{DUT}], [Y_{OPEN}] and [Y_{SHORT}].

2. The parallel elements Y_{PGS}, Y_{PGD} and Y_{PDS} can be extracted from the [Y_{OPEN}] as

$$Y_{PGS} = Y_{11,OPEN} + Y_{12,OPEN} \tag{3.1}$$

$$Y_{PGD} = -Y_{12,OPEN} \tag{3.2}$$

$$Y_{PDS} = Y_{22,OPEN} + Y_{21,OPEN} . \tag{3.3}$$

3. Subtract the parallel parasitics from [Y_{DUT}] and [Y_{SHORT}]

$$Y_{DUT}^{Shunt} = Y_{DUT} - Y_{OPEN} \tag{3.4}$$

$$Y_{SHORT}^{Shunt} = Y_{SHORT} - Y_{OPEN} . \tag{3.5}$$

4. Convert Y_{DUT}^{Shunt} and Y_{SHORT}^{Shunt} to Z_{DUT}^{Shunt} and Z_{SHORT}^{Shunt}.

5. Subtract the series parasitics Z_G, Z_S and Z_D from Z_{DUT}^{Shunt} by

$$Z'_{DUT} = Z_{DUT}^{Shunt} - Z_{SHORT}^{Shunt} . \tag{3.6}$$

6. Convert Z'_{DUT} to S'_{DUT}.

3.2.2 De-embedding of Noise Parameters

To validate the noise modeling, an accurate noise measurement result is necessary. Based on the noise correlation matrix [10] and the representation transformation matrix [10], the impact of surrounding parasitics can be removed for the measured four noise parameters. The same S-parameter results as before ([S_{DUT}], [S_{OPEN}] and [S_{SHORT}]) need to be measured to perform the

noise de-embedding. The noise correlation matrix of the equivalent noise-free two-port block (shown in Fig. 2.4) can be represented by the four noise parameters as

$$C_A = 2kT \begin{bmatrix} R_n & \frac{NF_{min}-1}{2} - R_n Y_{opt}^* \\ \frac{NF_{min}-1}{2} - R_n Y_{opt} & R_n |Y_{opt}|^2 \end{bmatrix}, \tag{3.7}$$

where C_A is the correlation matrix, which can be used for the noise de-embedding calculation with the procedure below [11].

Each representation can be transformed into another by the matrix [10] and the translation equation is

$$\vec{C}_T = \vec{T} \cdot \vec{C} \cdot \vec{T}' , \tag{3.8}$$

where $\vec{C}$ is the matrix before translation, $\vec{C}_T$ is the translated matrix, $\vec{T}$ is the transform matrix and $\vec{T}'$ is the Hermitian conjugation (transpose and complex conjugate) of $\vec{T}$.

Table 3.1. Transformation matrix between 3 representations [10].

		Original Representation		
		Admittance	Impedance	*ABCD*
Resulting Representation	Admittance	$\begin{bmatrix} 1 & 0 \\ 0 & 1 \end{bmatrix}$	$\begin{bmatrix} Y_{11} & Y_{12} \\ Y_{21} & Y_{22} \end{bmatrix}$	$\begin{bmatrix} -Y_{11} & 1 \\ -Y_{21} & 0 \end{bmatrix}$
	Impedance	$\begin{bmatrix} Z_{11} & Z_{12} \\ Z_{21} & Z_{22} \end{bmatrix}$	$\begin{bmatrix} 1 & 0 \\ 0 & 1 \end{bmatrix}$	$\begin{bmatrix} 1 & -Z_{11} \\ 0 & -Z_{21} \end{bmatrix}$
	ABCD	$\begin{bmatrix} 0 & A_{12} \\ 1 & A_{22} \end{bmatrix}$	$\begin{bmatrix} 1 & -A_{11} \\ 0 & -A_{21} \end{bmatrix}$	$\begin{bmatrix} 1 & 0 \\ 0 & 1 \end{bmatrix}$

The noise de-embedding procedure is as follows:

1. Convert C_A matrix of the DUT to its C_Y correlation matrix by

$$C_Y = \vec{T} \cdot C_A \cdot \vec{T}' , \tag{3.9}$$

where $\vec{T}$ is calculated from the Y_{DUT} based on Table 3.1.

2. Calculate the admittance correlation matrix of OPEN by

$$C_Y^{OPEN} = 2kT \cdot \Re\{Y_{OPEN}\}. \tag{3.10}$$

3. Subtract parallel parasitics from Y_{DUT} and Y_{SHORT}

$$Y_{DUT}^{Shunt} = Y_{DUT} - Y_{OPEN} \tag{3.11}$$

$$Y_{SHORT}^{Shunt} = Y_{SHORT} - Y_{OPEN} . \tag{3.12}$$

4. De-embed C_Y by

$$C_{Y\_De} = C_Y - C_Y^{OPEN} . \tag{3.13}$$

5. Convert Y_{DUT}^{Shunt} and Y_{SHORT}^{Shunt} to Z_{DUT}^{Shunt} and Z_{SHORT}^{Shunt}.

6. Convert C_{Y_De} to impedance representation by

$$C_Z = \vec{T} \cdot C_{Y\_De} \cdot \vec{T}' , \tag{3.14}$$

where $\vec{T}$ is calculated from the Z_{DUT}^{Shunt} based on Table 3.1.

7. Calculate the impedance correlation matrix of SHORT by

$$C_Z^{SHORT} = 2kT \cdot \Re\{Z_{SHORT}^{Shunt}\}. \tag{3.15}$$

8. Subtract the series parasitics from Z_{DUT}^{Shunt} by

$$Z'_{DUT} = Z_{DUT}^{Shunt} - Z_{SHORT}^{Shunt}. \tag{3.16}$$

9. Convert Z'_{DUT} to *ABCD* representation A'_{DUT}.

10. De-embed C_Z by

$$C_Z' = C_Z - C_Z^{SHORT} \ . \tag{3.17}$$

11. Convert C_Z' to C_A' by

$$C_A' = \vec{T} \cdot C_Z' \cdot \vec{T}' \ , \tag{3.18}$$

where $\vec{T}$ is calculated from the A_{DUT}' based on Table 3.1.

Therefore, the four noise parameters of an intrinsic transistor can be calculated from the noise correlation matrix C_A' by

$$NF_{min} = 1 + \frac{1}{kT}\left(\Re\{C_{A,12}'\} + \sqrt{C_{A,11}'C_{A,22}' - (\Im\{C_{A,12}'\})^2}\right) \tag{3.19}$$

$$Y_{opt} = \frac{\sqrt{C_{A,11}'C_{A,22}' - (\Im\{C_{A,12}'\})^2} + j\Im\{C_{A,12}'\}}{C_{A,11}'} \tag{3.20}$$

$$R_n = \frac{C_{A,11}'}{2kT} \tag{3.21}$$

3.3 Conclusion

This chapter introduced the tuner-based high frequency noise measurement system and the de-embedding techniques for S-parameters and noise parameters. The measured results will be used for parameter extraction and high frequency noise model validation.

CHAPTER 4

NOISE CALCULATION OF BIPOLAR TRANSISTORS

This chapter discusses the noise sources modeling, the noise correlation analysis and the high frequency noise calculation of the bipolar transistors based on Y-parameter method. From the noise origin and device physics, the noise transit time is directly extracted from the compact model without the need for any noise measurement. Compared with the conventional experimental noise transit time extraction method, this methodology presents a more accurate extraction of noise transit time and better prediction of noise correlation. This research is focused on the advanced high speed SiGe HBT device with the f_T up to 115 GHz.

4.1 Noise Sources in SiGe HBTs

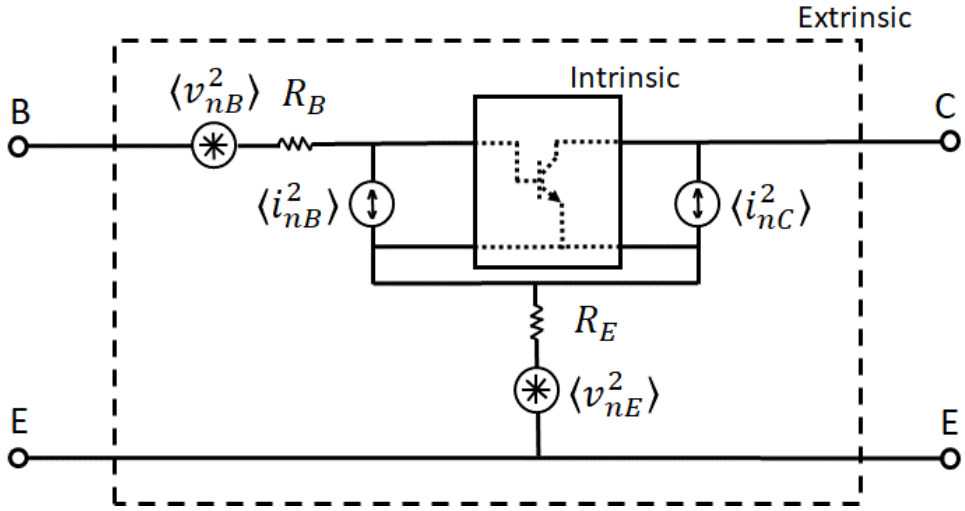

Figure 4.1. Y-parameter equivalent circuit for SiGe HBTs [9]. $\langle i_{nB}^2 \rangle$ and $\langle i_{nC}^2 \rangle$ are correlated.

---

[1] © 2018 IEEE. Portions reprinted or adapted, with permission from:
P. Cheng and H. Shichijo, "High frequency noise characterization and modeling of SiGe HBTs", in *IEEE Trans. Microw. Theory Techn.*, vol. 66, no. 12, pp. 5169–5175, Oct. 2018.

4.1.1 Thermal Noise Sources

For the SiGe HBT device, the high frequency noise is contributed by two kinds of noise sources: thermal noise and shot noise. As shown in Fig. 4.1, the thermal noise is mainly contributed from the base and emitter series resistances, which can be modeled as the noise voltage sources in series at the base and emitter terminals by

$$\langle v_{nE}^2 \rangle = 4kTR_E \cdot \Delta f \tag{4.1}$$

$$\langle v_{nB}^2 \rangle = 4kTR_B \cdot \Delta f\ , \tag{4.2}$$

where k is the Boltzmann's constant, T is the absolute ambient temperature and R_B and R_E are the terminal resistances of the transistors including the intrinsic and extrinsic parts.

4.1.2 Shot Noise Sources

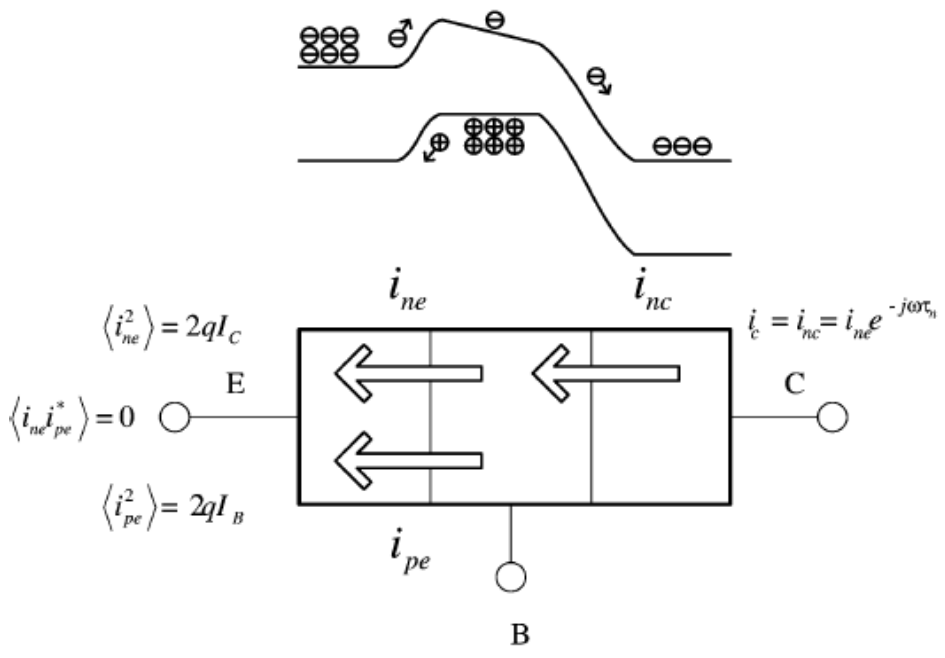

Figure 4.2. The origin of shot current noise [12].

As described in Chapter 2, the current shot noise is generated at the pn junction caused by the random process of the carrier's overcoming the potential barrier. However, in a bipolar device, the current shot noise is only significant at the EB (emitter-base) junction, because the CB (collector-base) junction is usually reverse-biased for low-noise purpose, where additional shot noise is negligible due to a drift process until the breakdown occurs. Therefore, one only needs to analyze the shot noise generated at the EB junction for the shot noise source modeling.

In the EB junction, the majority holes flowing from the base to the emitter across the junction causes the base current shot noise $2qI_b$, which is caused by the random process of carriers overcoming the potential barrier at the EB junction. Similarly, the majority electrons injected through the EB junction causes the shot current noise $2qI_c$.

Because the CB junction guarantees no additional shot noise because of a drift process, the current shot noise $2qI_c$ observed at the collector terminal is the transported noise current from the EB junction. The two shot-like noise currents generated at EB junction are described as [12]

$$\langle i_{pe}^2 \rangle = 2qI_B \tag{4.3}$$

$$\langle i_{ne}^2 \rangle = 2qI_c\,, \tag{4.4}$$

where $\langle i_{pe}^2 \rangle$ is caused by the hole current injection to the emitter and $\langle i_{ne}^2 \rangle$ is caused by the electron current injection to the base as illustrated in Fig. 4.2. The correlation of $\langle i_{pe}^2 \rangle$ and $\langle i_{ne}^2 \rangle$ is zero because the electron and hole injection are independent.

The collector current noise is described as the transport of $\langle i_{ne}^2 \rangle$ with a time delay τ_n

$$i_{nc} = i_{ne} e^{-j\omega\tau_n}\,, \tag{4.5}$$

where τ_n is the delay time associated with the transport of emitter-injected electron shot noise current.

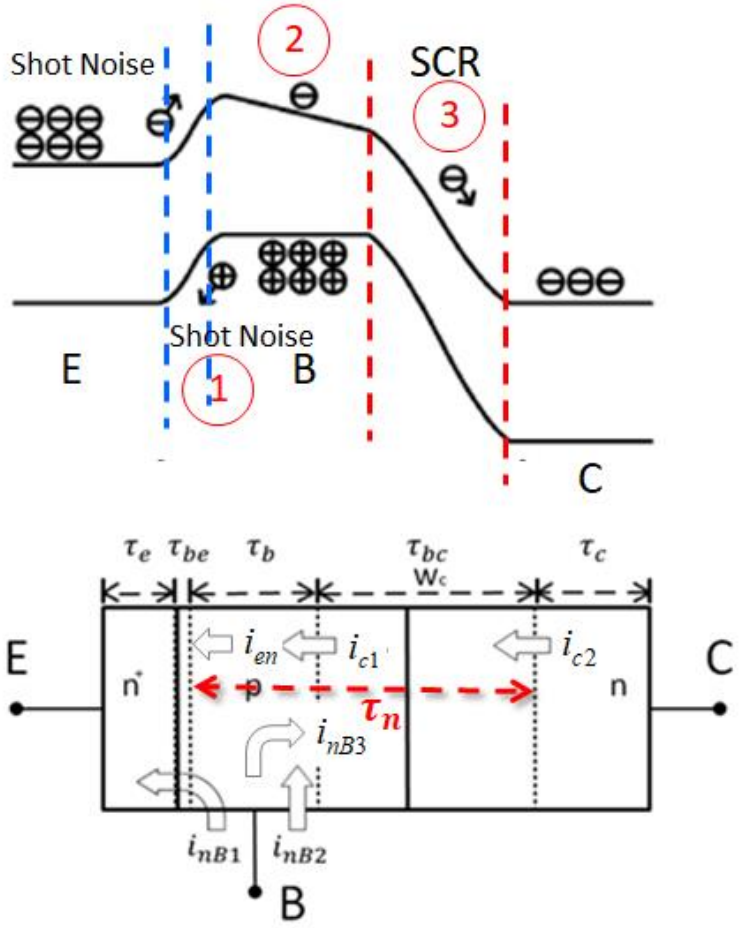

Figure 4.3. The origin of noise current correlation.

The base noise current is contributed by three elements corresponding to the three mechanisms shown in Fig. 4.3:

1. Noise induced by the velocity fluctuation of minority hole in the emitter (i_{nB1}).

2. Noise induced by the velocity fluctuation of minority electron in the base region (i_{nB2}). This hole noise current equals to the deviation of electron noise currents between the two sides of the neutral base region.

3. Additional base noise current due to the transport of electron noise current across the CB SCR (i_{nB3}), which is located at the end side of the neutral base region.

Therefore, the base shot noise current is correlated with the transported electron noise current with a time delay τ_n.

Based on the base and collector shot noise current models, the noise power density of the noise sources and shot noise cross-correlation in common-emitter configuration are given by the transport noise model [12] [13]

$$\langle i_{nB}^2 \rangle = [2qI_b + 4qI_c(1 - \Re\{e^{-j\omega\tau_n}\})] \cdot \Delta f \tag{4.6}$$

$$\langle i_{nC}^2 \rangle = 2qI_c \cdot \Delta f \tag{4.7}$$

$$\langle i_{nB}^* i_{nC} \rangle = 2qI_c(e^{-j\omega\tau_n} - 1) \cdot \Delta f\ , \tag{4.8}$$

where I_c and I_b are the dc collector and base current respectively and q is the electron charge. $\langle i_{nB}^* i_{nC} \rangle$ describes the cross-correlation of base and collector noise current, which is highly affected by the noise transit time τ_n.

4.2 Noise Transit Time

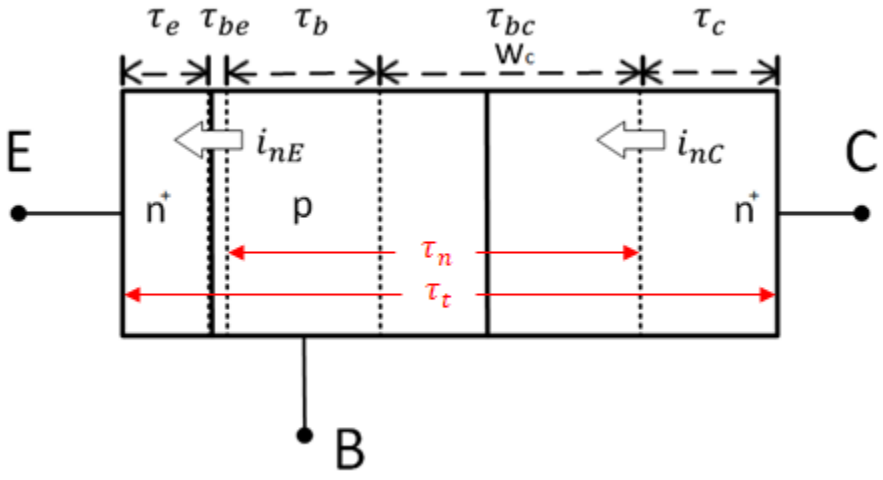

Figure 4.4. Transport noise model for SiGe HBTs [adopted from 12, 19].

As discussed in the last section, the shot noise is generated only at the EB junction, and the base current shot noise $2qI_b$ caused by the majority holes randomly crossing the potential barrier and the electron shot noise current at the EB junction are independent and not correlated. However, as the emitter electron noise current transports through the quasi-neutral base and the CB SCR (space charge region), it induces a hole density fluctuation in the base which gets added to the base current noise [14]. Therefore, it creates a correlation between the base current noise and collector current noise and the total time delay of the emitter electron noise current transported to the collector is described by noise transit time τ_n.

As the analysis by Prichard [15] shows, the base related delay time in the diffusion limited case is much smaller than the base transit time by a factor of 0.2. However, this excess phase shift factor should be modified to 0.7-0.8 because of the Ge grading effect on the base transit time [16] [17]. Therefore, in this dissertation an approximation of this factor to 1 is used to calculate the base related delay time. On the other hand, the base related delay time is not very critical since the base transit time is much smaller than the CB SCR transit time in modern SiGe HBTs, until they reach high-injection region.

As shown in the transport noise model, the noise transit time τ_n is critical to determine the correlation effect in the noise calculation and modeling. Therefore, the dependence of τ_n is discussed in this dissertation by characterizing the sample SiGe HBT device over temperature and bias.

The origin and location of EB noise generation are also studied by Decker et al. [18] using the simulation based on the Impedance Field Method. They have shown that the location of the generated electron noise is very close to the edge of the depletion region of the EB junction as

shown in Fig. 4.5. Therefore, it is reasonable to approximate τ_n as the sum of the neutral base transit time and the transit time across the collector-base junction SCR [19]. On the other hand, the transistor transit time τ_t is the sum of the time delay from the emitter to collector as shown in Fig. 4.4. (4.9)

$$\tau_n = \tau_b + \tau_{bc} \tag{4.10}$$

$$\tau_t = \tau_e + \tau_{be} + \tau_b + \tau_{bc} + \tau_c \,,$$

where τ_b, τ_c and τ_e are the time constant at the natural base, collector and emitter respectively; τ_{bc} and τ_{be} are the time delay at the SCR at base-collector and base-emitter, respectively.

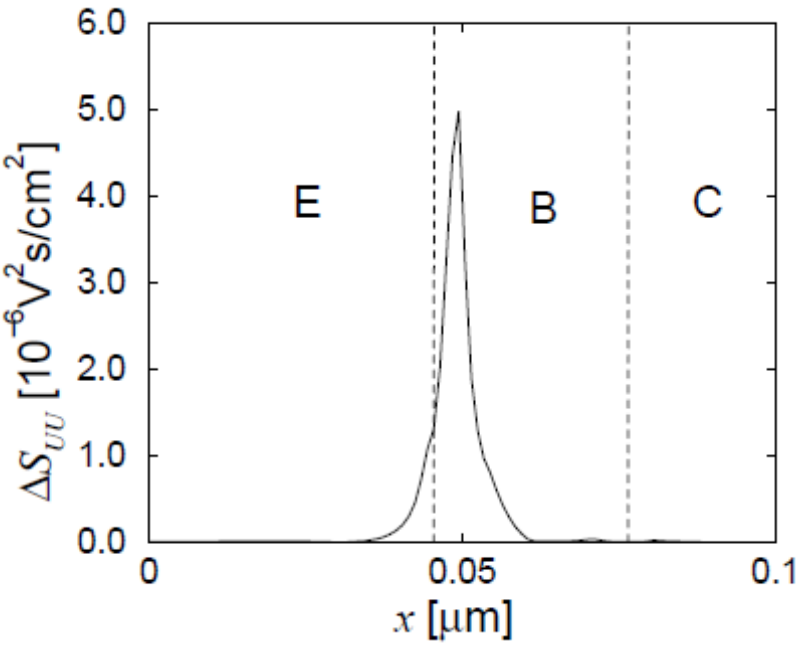

Figure 4.5. Electron noise power originates near the EB junction [18].

To normalize τ_n we define a parameter, noise ratio, which is equal to τ_n/τ_t. Typically, τ_t can be calculated from $1/2\pi f_T$, where f_T is the current cutoff frequency of the transistor, which can be extracted by S-parameter measurement.

As illustrated in the Fig. 4.6, the noise correlation affects both the value and slope of the NF_{min} over the frequency. The value and slope of NF_{min} are both decreasing with larger noise ratio. Therefore, the noise ratio needs to be well characterized for accurate noise modeling especially at high frequency range.

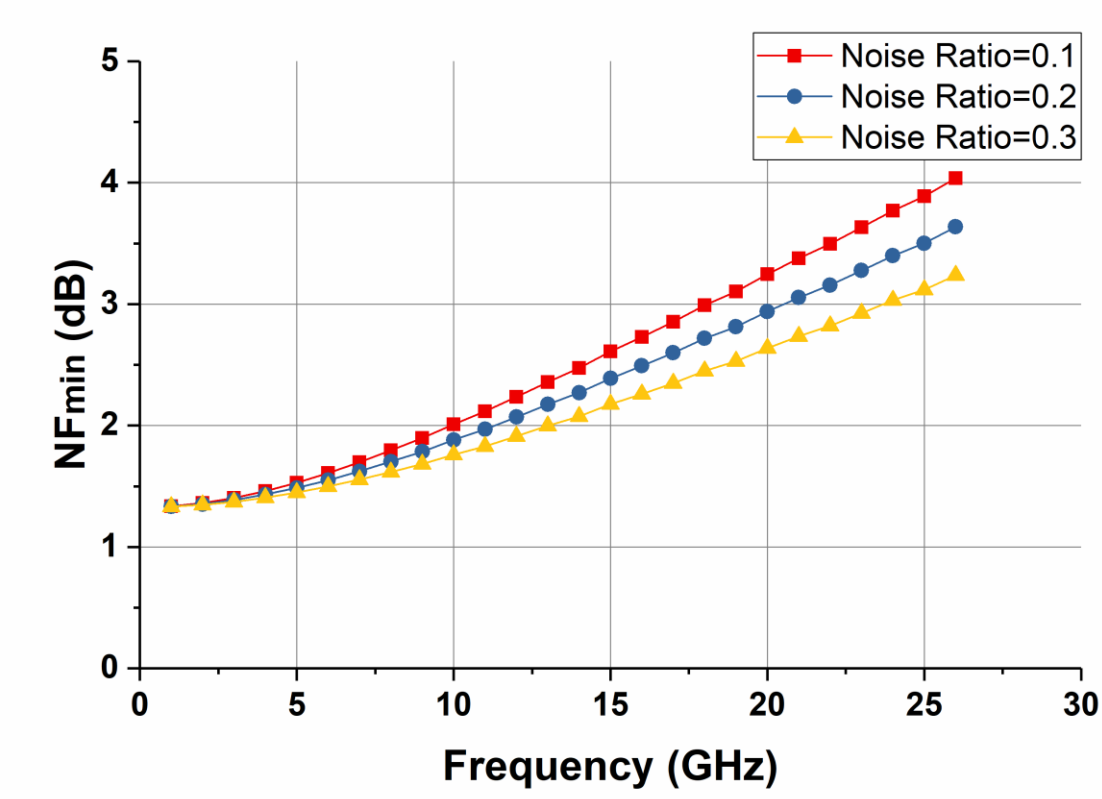

Figure 4.6. The effect of noise ratio of NF_{min} for a sample SiGe HBT at $V_{be} = 0.9V$ and $V_{ce} = 1V$ at room temperature.

Some papers proposed methods for the experimental extraction of the noise transit time, but the extraction results are either not accurate or hard to measure. Yau and Voinigesou describe

a method in [9] where the noise transit time can be obtained from the slope of the phase of transconductance vs frequency

$$\tau_n = -\frac{\partial}{\partial\omega} phase[g_m(\omega)]\,. \tag{4.11}$$

Based on the extraction method in [20], the transconductance g_m is given by

$$g_m = \frac{1-|A_c|}{|A_c|}\left(\frac{1}{R_\pi} + j\omega C_\pi\right) \tag{4.12}$$

$$R_\pi = \Re\left\{\frac{A_{c,11}|A_c|}{A_{c,12} - |A_c|R_{bi}}\right\}, \tag{4.13}$$

where $[A_c]$ is the *ABCD* matrix of the intrinsic part of the HBT which can be calculated from the measured S-parameter data, R_{bi} is the intrinsic base resistance and C_π is calculated from the slope of $Im(\frac{A_{c,12}}{|A_c|})$ when plotted versus $1/\omega$. The value of τ_n extracted by this method is almost equal to the total time delay from emitter to collector.

A similar method is discussed in [21]. They extract the transit time from the phase delay of the emitter and collector current gain by modeling it as a low-pass function

$$\alpha(f) = \alpha_0 \frac{e^{-j\omega\tau}}{1 + j\frac{f}{f_\beta}}, \tag{4.14}$$

where α is defined as the transport factor and can be extracted from the Z-parameters by

$$\alpha = \frac{Z_{12} - Z_{21}}{Z_{22} - Z_{21} - R_c}\,. \tag{4.15}$$

Then one can calculate the τ at low frequency by

$$\tau = -\frac{d\left(phase\big(\alpha(f)\big)\right)}{d\omega}\,. \tag{4.16}$$

This method also gets a delay time very close to the total transit time from emitter to collector which is calculated from $1/2\pi f_T$ as shown in Fig. 4.7.

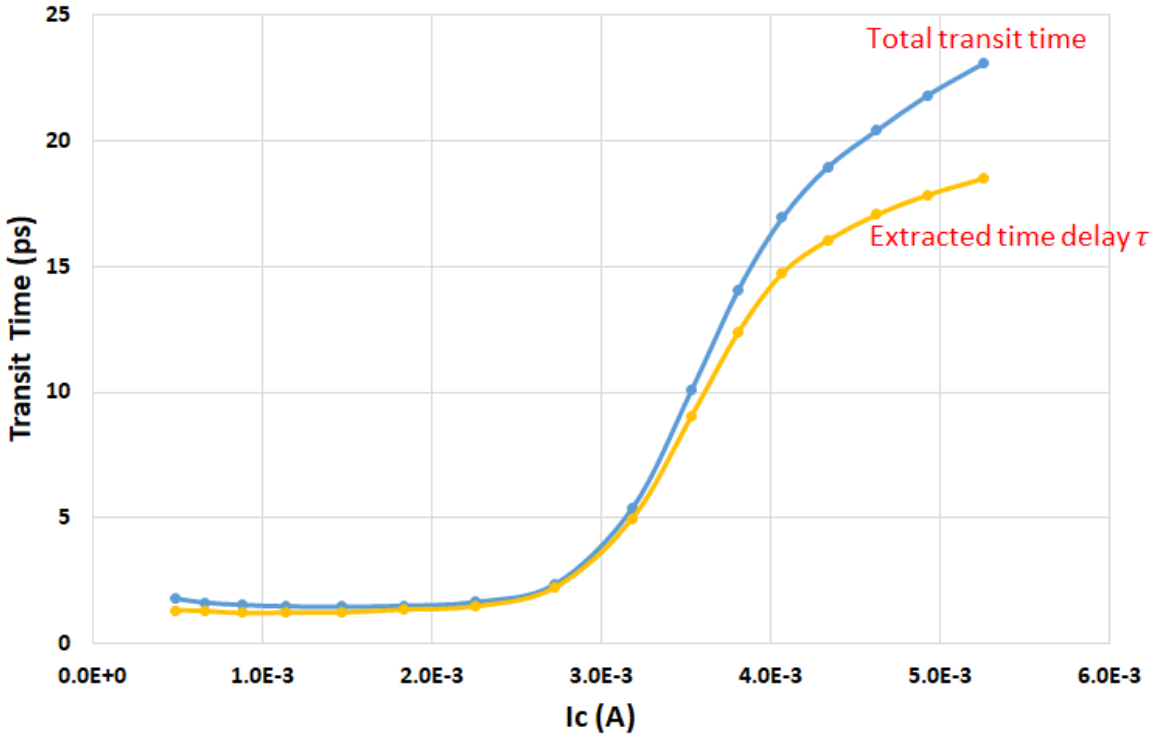

Figure 4.7. Extracted transit time based on Basaran's method [21] applied to our SiGe HBT.

Also, in the papers [22] [23], they characterize the noise transit time by fitting the NF_{min} between the calculated noise from model and the measured noise parameters. For this kind of extractions, it still needs the tuner-based noise measurement as well as it needs an accurate noise measurement result which is hard to implement compared with the S-parameter measurement. However, this method can still give a reference for the extraction method.

In addition to these methods, in [24], they extract the noise transit time directly from the Z-parameters. This kind of extraction cannot give an accurate result because the analysis of time constant is oversimplified and needs too many assumptions for the small-signal equivalent circuit.

This method is also over-estimating the noise transit time, which is almost equal to the total transit time from emitter to collector.

In conclusion, one needs to explore an accurate and easily approachable methodology to extract the noise transit time. Therefore, we have developed an extraction method based on the HICUM compact model.

4.3 Extraction of Noise Transit Time from HICUM Model

We now discuss the methodology of extracting τ_n based on parameters from the HICUM compact model [25]. The parameters used in the noise transit time extraction are based on the HICUM v2.3 model.

Since the time delay constants of the transistor are highly dependent on the bias conditions, we need to separate the operating conditions to low-current region, medium- and high-current regions with the assumption that at the low-current region the time constants are only voltage dependent and at the medium- and high-current regions the time constants are both voltage and current dependent.

In the low-current region, the low-current transit time τ_0 and the bias independent low-current emitter time constant τ_{Ef0} are given in the model.

In the medium to high current region, with the increasing of I_c, the time constants in the natural collector and neutral emitter increase. Therefore, there is an additional time delay $\Delta\tau_{fh}$ in neutral base and collector regions and $\Delta\tau_{Ef}$ in the neutral emitter region given by [26]

$$\Delta\tau_{fh} = \tau_{hcs} w^2 \left[1 + \frac{2I_{CK}}{I_C\sqrt{i^2 + a_{hc}}}\right] \tag{4.17}$$

$$\Delta\tau_{Ef} = \tau_{Ef0}(I_C/I_{CK})^{g_{\tau E}}\,, \tag{4.18}$$

where τ_{hcs} is the collector saturation transit time, w is the collector current dependent injection region width, I_{CK} is the Kirk-effect current, $g_{\tau E}$ is the exponent factor for current dependence of neutral emitter storage time, $i = 1 - I_{CK}/I_C$ and a_{hc} is the smoothing factor.

At medium to high current densities, the base-collector space charge region (SCR) becomes quasi-neutral, which is the so-called Kirk-effect. To describe the effect, a continuously differentiable current I_{CK} can be written as [26]

$$I_{CK} = \frac{v_{ceff}}{r_{Ci}} \frac{1}{\sqrt{1 + (v_{ceff}/V_{lim})^2}} \left[1 + \frac{x + \sqrt{x^2 + 10^{-3}}}{2}\right] \tag{4.19}$$

$$x = \frac{v_{ceff} - V_{lim}}{V_{PT}}, \tag{4.20}$$

where v_{ceff} is the effective collector voltage, and r_{Ci} is the low-field internal collector resistance. The v_{ceff} is given by the smoothing function with v_{CEi} and v_{CEs} as

$$v_{ceff} = V_T \left[\ln\left(1 + \exp\left(\frac{v_{CEi} - v_{CEs}}{V_T} - 1\right)\right) + 1\right]. \tag{4.21}$$

The temperature dependence of r_{Ci}, τ_0 and τ_{hcs} is determined by a few parameters in the model respectively [26]

$$r_{Ci}(T) = r_{Ci0}\left(\frac{T}{T_{ref}}\right)^{\zeta_{Ci}} \tag{4.22}$$

$$\tau_0(T) = \tau_0(1 + \alpha_{\tau 0}(T - T_{ref}) + K_{\tau 0}(T - T_{ref})^2) \tag{4.23}$$

$$\tau_{hcs}(T) = \tau_{hcs0}\left(\frac{T}{T_{ref}}\right)^{\zeta_{Ci}-1}, \tag{4.24}$$

where $\alpha_{\tau 0}$ and $K_{\tau 0}$ are the first and second order temperature coefficients of reference temperature T_{ref}, and ζ_{Ci} is the temperature exponent factors of the mobility of the internal collector region.

Making the collector current dependent injection region width w as a continuous function of current can avoid the charge stored (minority holes injected into collector) becoming nonphysical at $I_C < I_{CK}$. The collector current dependent injection region width is then described by

$$w = \frac{i + \sqrt{i^2 + a_{hc}}}{1 + \sqrt{1 + a_{hc}}}, \tag{4.25}$$

where a_{hc} is the smoothing factor for current dependence of base and collector transit time.

Based on the equations (4.17) and (4.18), the biasing dependent additional time constant $\Delta\tau_{fh}$ and $\Delta\tau_{Ef}$ can be calculated from the model. Then we can calculate the noise ratio based on the definition $noise\ ratio = \tau_n/\tau_t$ as follows.

Based on the definition and device physics we presented in Chapter 4, section 4.2, the total transistor transit time τ_t is the sum of low-current transit time and the additional time delays at neutral emitter, base and collector

$$\tau_t = \tau_0 + \Delta\tau_{fh} + \Delta\tau_{Ef} \tag{4.26}$$

and the noise transit time τ_n is obtained by subtracting τ_{Ef0}, $\Delta\tau_{Ef}$ and the additional time delay in the neutral collector $f_{\tau hc}\Delta\tau_{fh}$ from the transistor transit time τ_t

$$\tau_n = \tau_t - \left(\tau_{Ef0} + \Delta\tau_{Ef} + f_{\tau hc}\Delta\tau_{fh}\right). \tag{4.27}$$

The noise ratio is then given by [27, 28]

$$noise\ ratio = \frac{\left(\tau_t - \tau_{Ef0} - \Delta\tau_{Ef} - f_{\tau hc}\Delta\tau_{fh}\right)}{\tau_t}, \tag{4.28}$$

where $f_{\tau hc}$ is a partition parameter (default is 0.6) of the time delay between the base and collector components at high-current region. τ_{be} is ignored since its contribution is usually small in the bias range of interest.

Table 4.1. The HICUM model parameters for noise transit time extraction.

	Parameter Name	Description of the parameter
Group 1	τ_0	Low-current transit time
	τ_{Ef0}	Bias independent low-current emitter constant
	τ_{hcs}	Saturation time constant at high current densities
Group 2	V_{CEs}	Internal C-E saturation voltage
	V_{lim}	Voltage separating ohmic and saturation velocity regime
	V_{PT}	Collector punch-through voltage
Group 3	$f_{\tau hc}$	Partitioning factor for base and collector portion
	$g_{\tau E}$	Exponent factor for current dependence of neutral emitter storage time
	a_{hc}	Smoothing factor for current dependent of base and collector transit time
	r_{Ci0}	Internal collector resistance at low electric field
Group 4	$\alpha_{\tau 0}$	The first order temperature coefficient
	$K_{\tau 0}$	The second order temperature coefficient
	ζ_{Ci}	Temperature exponent for r_{Ci0}

The model parameters used in the noise transit time extraction are from the HICUM v2.3 model summarized in Table 4.1.

As an example, Fig. 4.8 is the extracted noise ratio from the HICUM model parameters of a sample SiGe HBT device over the collector current density. The noise ratio is the key parameter for noise correlation prediction for bipolar transistors.

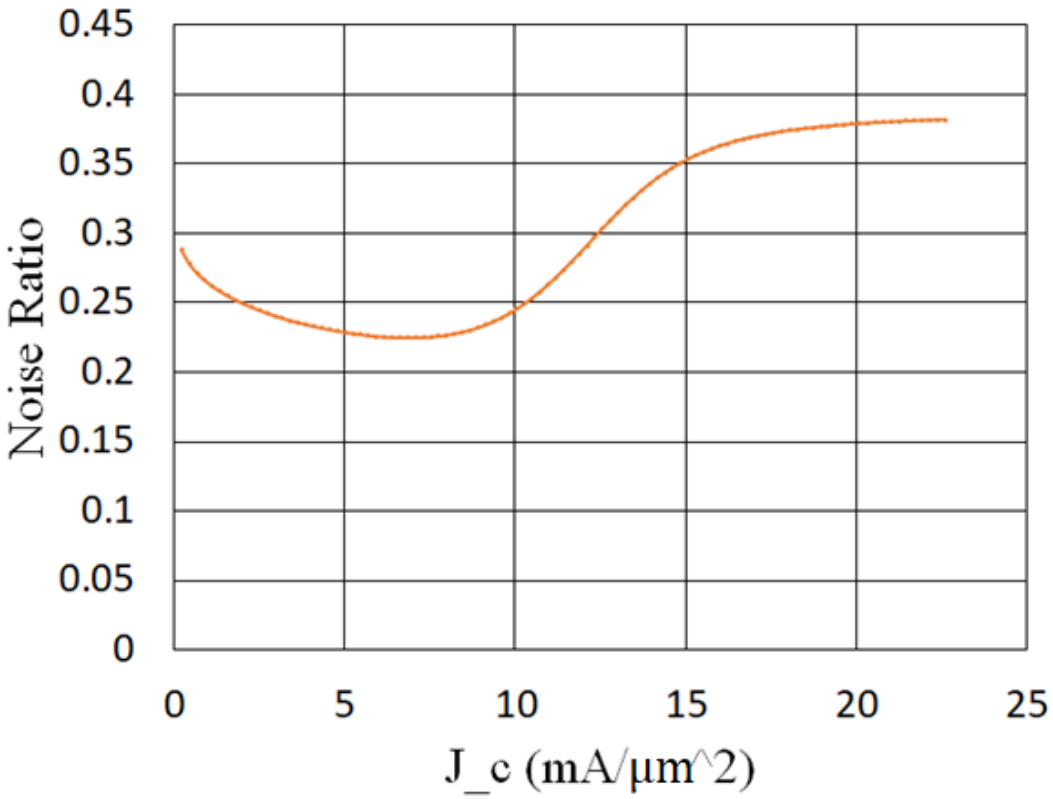

Figure 4.8. Extracted noise ratio for the sample SiGe HBT over the J_C.

4.4 Resistances Extraction for SiGe HBTs

Base resistance and emitter resistance of the bipolar device affect the transistor's four noise parameters, especially the base resistance which is at the input of the device. Therefore, it is

important to extract the access resistances at the base and emitter terminals. In the past, people proposed many methods to accurately extract the resistances of transistor from dc or ac measurement. In this chapter, we will discuss the methods we selected to extract the base and emitter resistances from the measurement data.

4.4.1 Emitter Resistance Extraction

The emitter resistance can be extracted from the Z-parameter data which is transformed from the measured S-parameter data in low frequency range (typically under 5 GHz). It is obtained from the intercept of $\Re(Z_{12})$ versus $1/I_c$ curve [29]. The equivalent circuit is shown in Fig. 4.9.

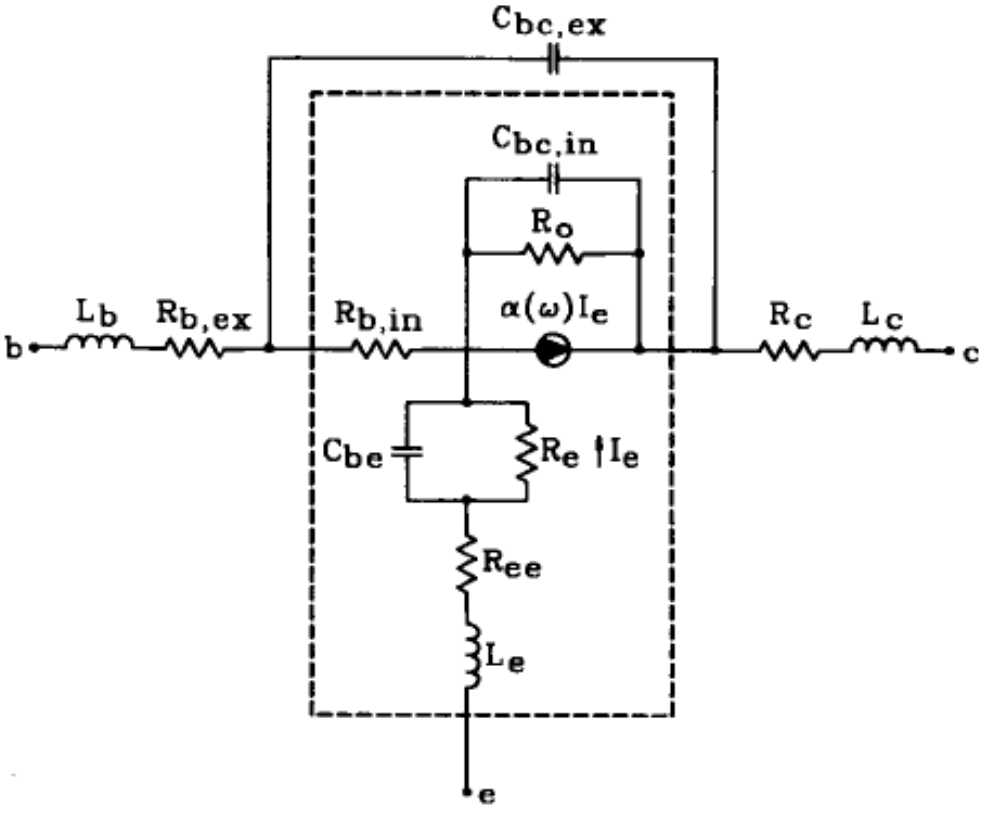

Figure 4.9. Equivalent circuit for emitter resistance extraction [29].

At a very low frequency (below 5GHz), the circuit can be simplified to a simple T-type circuit, where the real part of Z_{12} is equal to $R_e + R_{ee}$. R_e can be presented by the transconductance as

$$R_e \approx \frac{1}{g_m} = \frac{kT}{qI_C}. \tag{4.29}$$

Then we can obtain the emitter resistance by

$$\Re(Z_{12}) \approx \frac{kT}{qI_C} + R_{ee}, \tag{4.30}$$

where R_{ee} is the emitter resistance used for RF noise calculation.

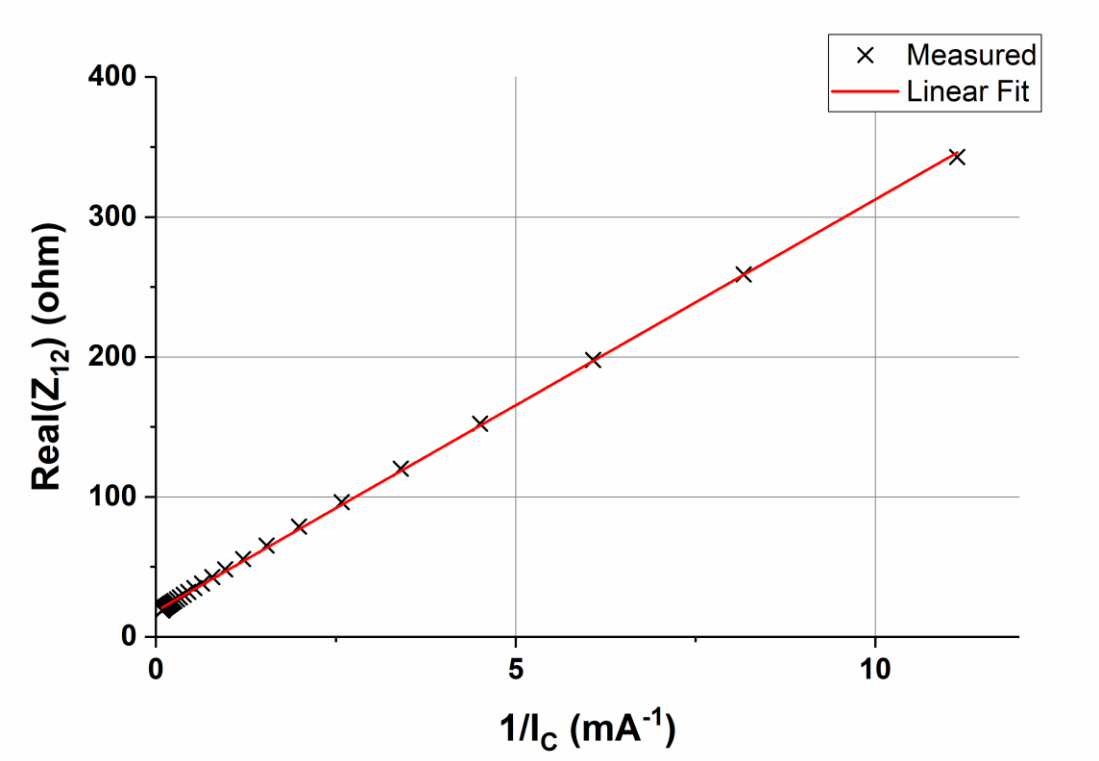

Figure 4.10. Extracted emitter resistance for the sample SiGe HBT.

Figure 4.10 shows the emitter resistance extraction result of a sample SiGe HBT device. The extracted value is 16.2 ohm. Kraus and Schröter [30] mention that this low-frequency small-

signal method we have used can eliminate the constraint of high-injection and the impact of self-heating and gives similar results to the g_m method and therefore should be acceptable.

The emitter resistance can also be extracted by the method from [31],

$$R_E = \frac{\Im\{h_{11}\}}{\Im\{h_{21}\}} - \frac{1}{g_m} \tag{4.31}$$

$$with\ \frac{1}{g_m} = \Re\left\{\frac{1}{h_{21}}\right\} \cdot \frac{V_T}{I_{bei}}, \tag{4.32}$$

where H-parameters are obtained from the Y-parameters after removing the transfer branches using utilitarianized S-parameters [31]. By plotting $\frac{1}{g_m}$ vs $\frac{\Im\{h_{11}\}}{\Im\{h_{21}\}}$ over base biasing current at 2 GHz, the R_E can be obtained from the intercept.

As shown in Fig. 4.11, the extracted R_E value by this method is around 16 ohm.

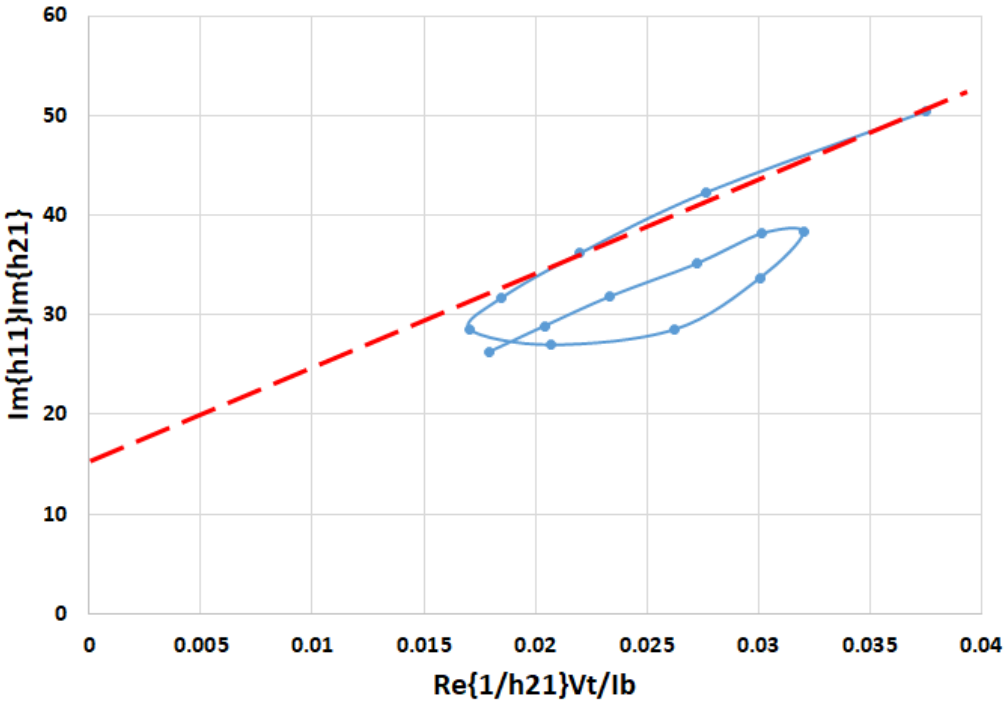

Figure 4.11. Extracted emitter resistance for the sample SiGe HBT.

4.4.2 Base Resistance Extraction

Various methods for the base resistance extraction are proposed in the literatures [32, 33]. In this section, we introduce and demonstrate these extraction methods based on a sample SiGe HBT transistor.

Usually, the base resistance is divided into an intrinsic part R_{Bi} and an extrinsic part R_{Bx}

$$R_B = R_{Bi} + R_{Bx}\,, \tag{4.33}$$

where R_{Bx} is independent of the bias condition and temperature but R_{Bi} is dependent on the bias condition and temperature.

In this section, we discuss three main methods to determine the base resistance: tetrode test structure, Impedance Circle and H-parameters.

In paper [34], Schroter and Lehmann indicate the method that uses the data from the dc measurement of a rectangular tetrode test structure to determine the base resistance of the bipolar transistor. Based on the device physics and layout, the normalized resistance between the two base contacts can be written as

$$R_B = R_{sBi}\frac{w}{L_e} + R_{Bx}\,, \tag{4.34}$$

where R_{sBi} is the intrinsic base sheet resistance, R_{Bx} is the extrinsic base resistance, w is emitter width and L_e is the effective emitter length. R_{sBi} and R_{Bx} can be determined by the linear regression of customized test tetrodes data with different emitter width w. Then the base resistance can be calculated based on the geometry of the bipolar transistor. For this sample SiGe HBT device, the extracted value of base resistance by this method is 380 ohm which is over-estimated comparing with model fitted data and other $R_B$extraction results as discussed below.

In [32], an impedance circle method is proposed to determine the base resistance. This method is based on the model and calculation on the H-parameters. The real and imaginary parts of H_{11} are described as

$$x = \Re(H_{11}) = R_B + \frac{g_{be}}{g_{be}^2 + (\omega C_i)^2} \tag{4.35}$$

$$y = \Im(H_{11}) = -\frac{\omega C_i}{g_{be}^2 + (\omega C_i)^2}, \tag{4.36}$$

where the contour plot of the $\Re(H_{11})$ and $\Im(H_{11})$ at different frequencies can be a semi-circle with the center of the circle equal to $R_B + 1/2g_{be}$ and the radius of the circle equal to $1/2g_{be}$. By fitting the circle equation to the impedance circle contour, the intercept of the circle is the base resistance. Fig. 4.12 shows the extraction result of the sample SiGe HBT by this method.

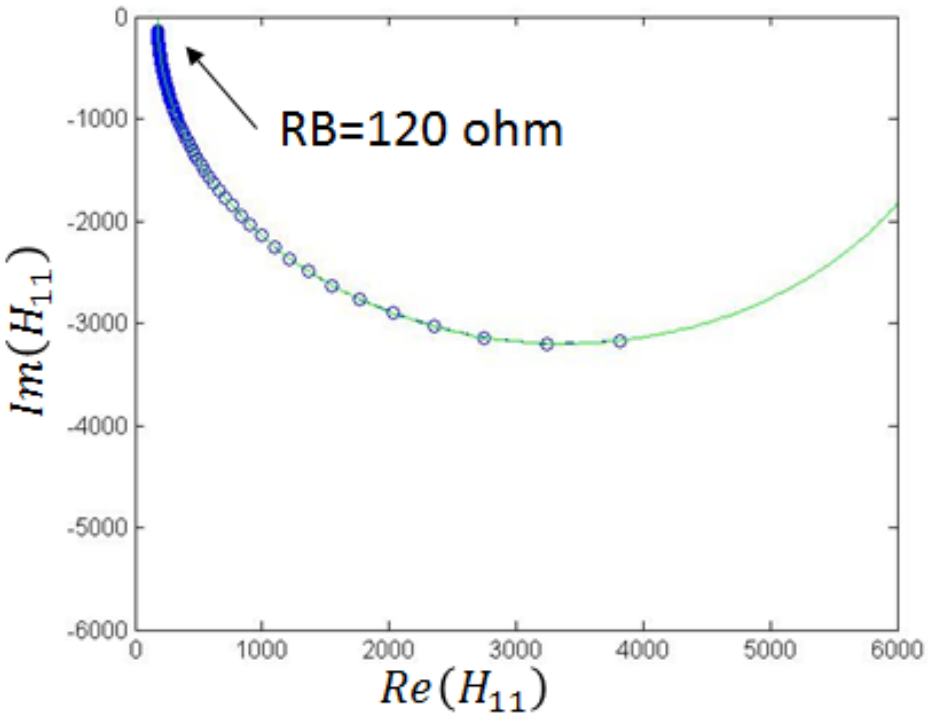

Figure 4.12. Impedance circle base resistance extraction for the sample SiGe HBT.

Another R_B extraction method is used to validate the results. R_B can be obtained from the high freqeuncy region of the real part of H_{11} parameter. As shown Fig 4.13, the measured R_B value is 120 ohm. Comparing the measured R_B with the simulated results from HICUM model, we find that the model overestimates the base resistance by about 50 ohm, which can affect the noise figure modeling as well as the other three noise parameters. The discrepancy between the measured and simulated values is most likely due to the device variations since the simulation model is only for nominal device.

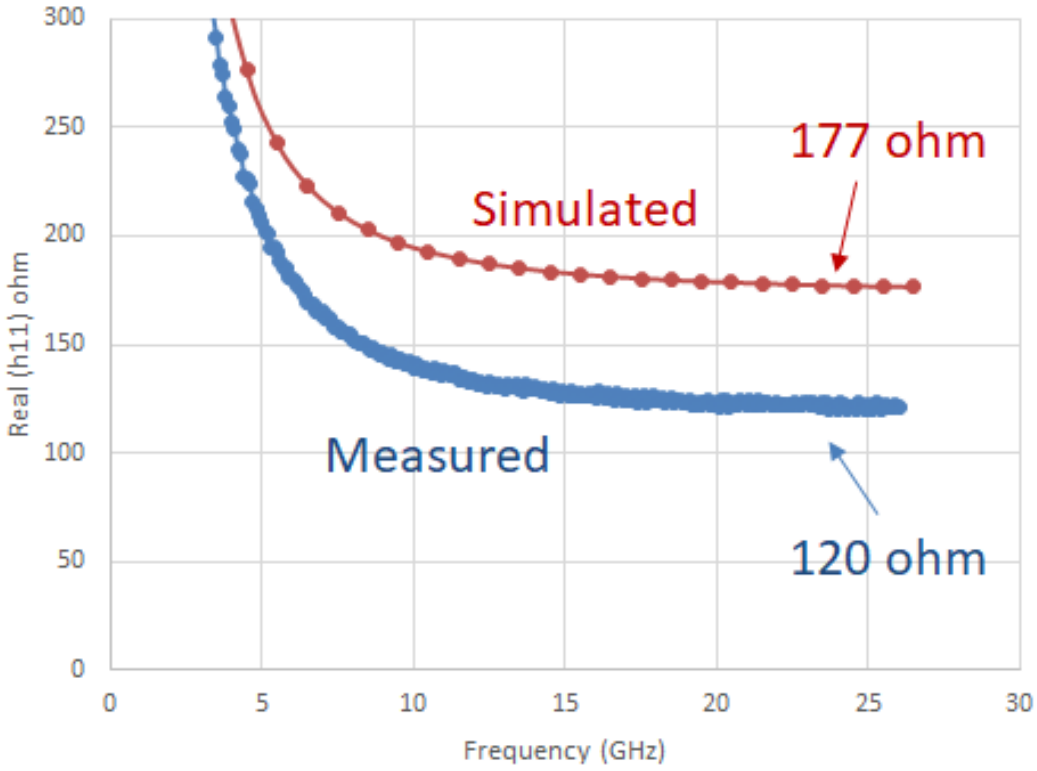

Figure 4.13. Base resistance extraction based on H-parameters for the sample SiGe HBT.

The bias and temperature dependences of R_B at $V_{ce} = 1\ V$ are shown in Fig. 4.14 at room temperature (25 °C) and $V_{be} = 0.9$ V. We have applied the circle impedance method [32] to the

simulated S-parameter data from HICUM model, and the extracted R_B shows an excellent fit to the model card operating point values over bias and temperature, verifying the validity of the method. The discrepancy between the measured and simulated values is again attributed to the device variation.

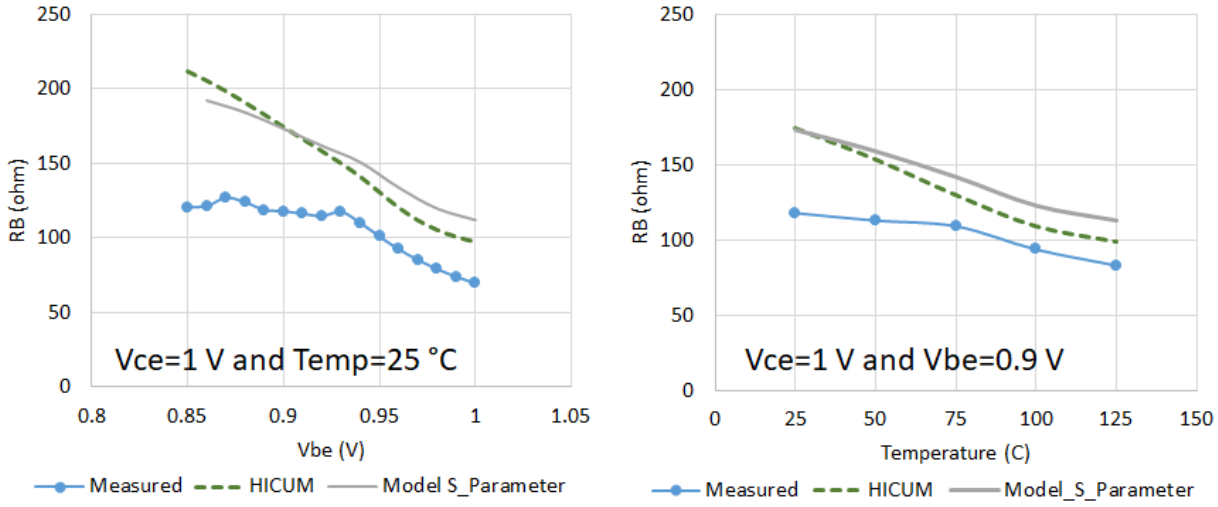

Figure 4.14. Temperature and bias dependence of base resistance for the sample SiGe HBT.

In conclusion, the rectangular test tetrode method can give a more straightforward prediction of the physical values for the base resistance as well as the extracted parameters can be used for bias and temperature dependence modeling of the intrinsic base resistance. But it needs a good geometry function to link the test tetrode to the actual device, which usually have some errors. The impedance circle method is based on the measured H-parameters which are simple to achieve from the S-parameter measurement. At the same time, this method can give a reasonable and accurate R_B extraction results.

4.5 Noise Calculation for SiGe HBTs

So far, we have extracted the noise transit time to calculate the shot noise sources and correlation effect in the transport noise model (equations from (4.6) to (4.8)) and the base and emitter resistances to calculate the thermal noise sources. Then these internal noise sources are transformed to the input of the device as an equivalent voltage noise source and an equivalent current source with a noise-free two-port Y-parameter block based on the Y-parameter method discussed in reference [9]. Then the four noise parameter can be calculated based on the theory in Section 2.6.

In summary, the entire high frequency noise calculation procedure for the SiGe HBT transistor is given by

1. Measure the S-parameter and dc data with a common emitter bias of the device under test (DUT).
2. Measure the S-parameters data of OPEN/SHORT dummy structures.
3. De-embed the measured S-parameter data of the DUT based on the OPEN/SHORT dummy structures.
4. Calculate the noise transit time of the DUT based on the extracted HICUM model parameters.
5. Extract the base and emitter resistances of the DUT from the de-embedded S-parameter data.
6. Calculate the internal noise sources and transform them to the input of the two-port block based on the Y-parameter method.

7. Calculate the four noise parameters of the DUT based on the two-port noise calculation theory.

4.6 Experimental Results

The utility of these calculation methodologies of noise transit time and high frequency noise properties has been validated using experimental data of SiGe HBTs. The SiGe HBTs use a 130 nm BiCMOS process with emitter dimensions of 0.15x1.77 μm^2 and f_T/f_{max} of approximately 110/160 GHz. Based on the measurement data, we present the model extraction, noise calculation and measurement results in this section.

The tuner-based noise measurement setup consists of a Maury MT983BL automated tuner, an HP 8970B noise figure meter set and an Agilent PNA (E8361C) as shown in Section 3.1. The system is controlled by Maury software ATSv5. To eliminate the effect of parasitic elements from the pads, we do the de-embedding using open/short dummy structures for both the measured S-parameter and noise parameter data [11]. The RF probes used in the on-wafer measurement have a 150μm pitch width, which are manufactured by Cascade Microtech.

Based on the extraction method described in Section III, we can calculate the noise transit time τ_n and noise ratio from the HICUM model. To validate the extraction results, we have measured the full noise properties of the SiGe HBT and obtained the τ_n and noise ratio by fitting the NF_{min} between the tuner-based measurement and Y-parameter calculation over bias, temperature, size and scaling generation.

From the measured temperature dependence of Gummel Plot in Fig. 4.15 we can find that I_b and I_c increase, but beta decreases with temperature. The decrease of beta with temperature is

a unique characteristic of SiGe HBT compared to silicon bipolar transistor and is a result of the bandgap narrowing in the heavily-doped base region [35]. The measured I_b and I_c are used in the high frequency noise calculation.

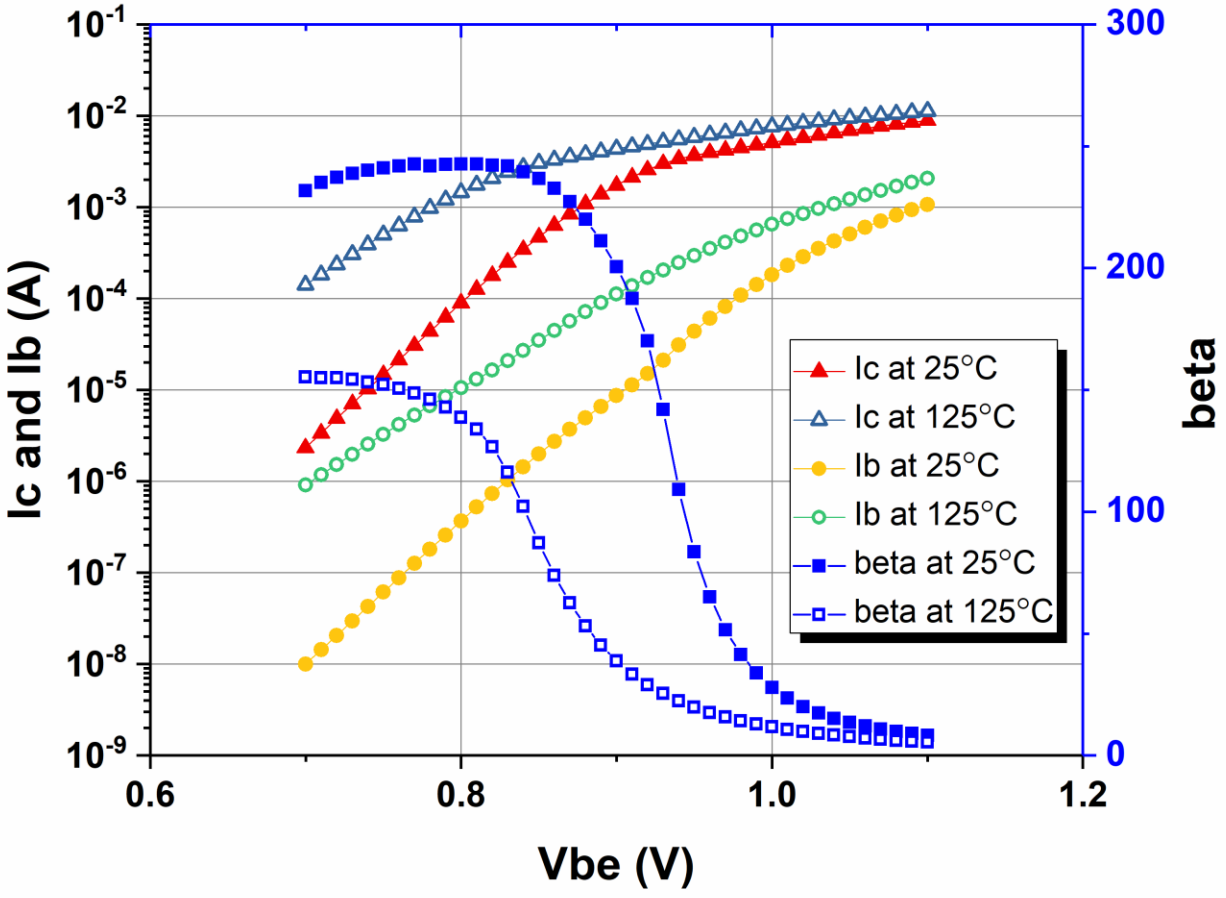

Figure 4.15. Measured temperature dependence of Gummel Plot.

Fig. 4.16 shows the simulated f_T vs V_{be} over the temperature for the sample SiGe HBT device. We can find that as the temperature increases, the peak f_T gets lower and moves to low V_{be} region.

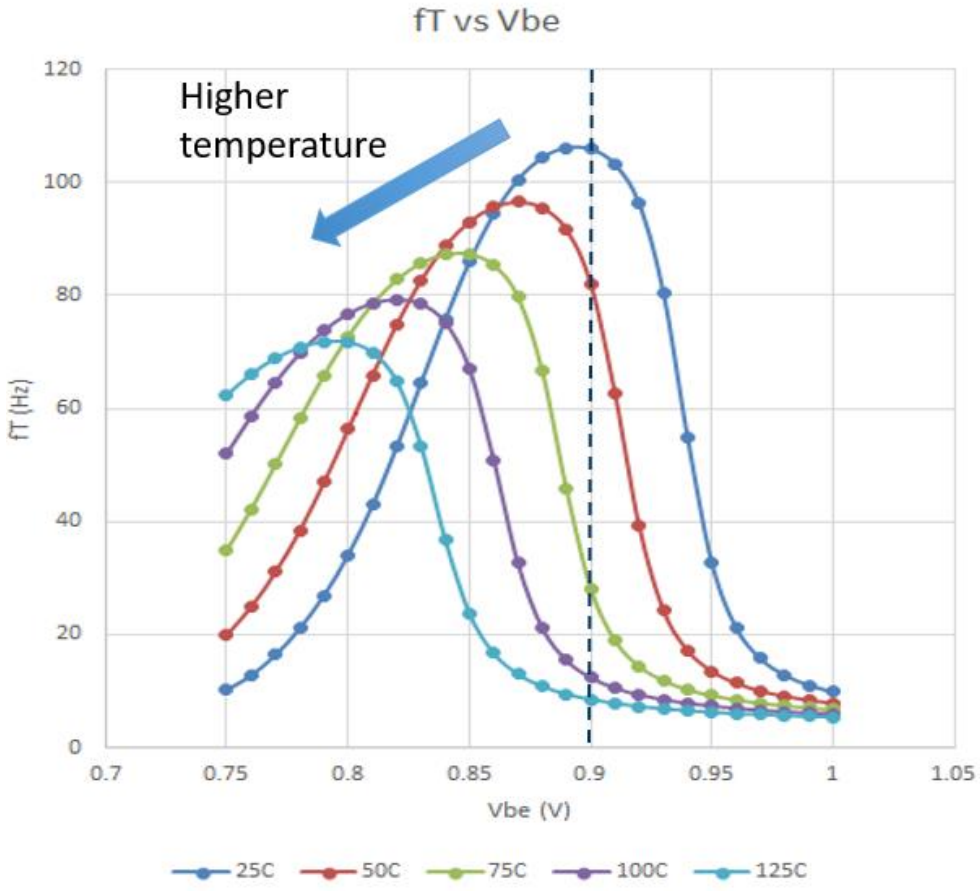

Figure 4.16. Simulated f_T vs V_{be} over the temperature for the sample SiGe HBT.

Fig. 4.17 shows the comparison of measured and modelled S11 and S22 for 1 GHz to 18 GHz sweep with $V_{ce} = 1\,V$, $V_{be} = 0.9\,V$ at room temperature. We find that the modelled S11 deviates from the measured, which can be explained by the discrepancy in the extracted base resistance by about 50 ohm from the modelled data as shown in Fig. 4.13. But it does not change the conclusion of our analysis, because the effect of the base resistance thermal noise is properly accounted for from the extracted (measured) base resistance. Since the device is small (0.15×1.77 μm^2), the S11 and S22 are close to SHORT in the frequency range.

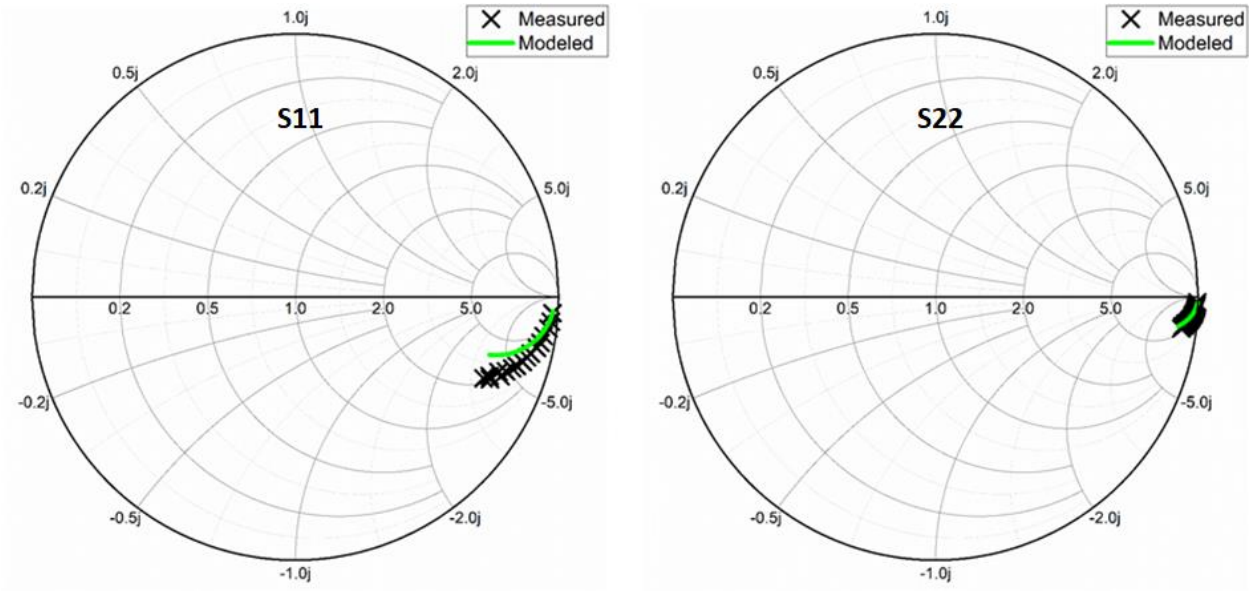

Figure 4.17. Measured vs simulated S11 and S22 for the sample SiGe HBT.

We have also compared the S21 between the modelled and measured data as shown in Fig. 4.18. The real part of the simulated S21 is matched with the measured data. But the imaginary part of the simulated S21 is deviated from the measured data especially at high frequency region.

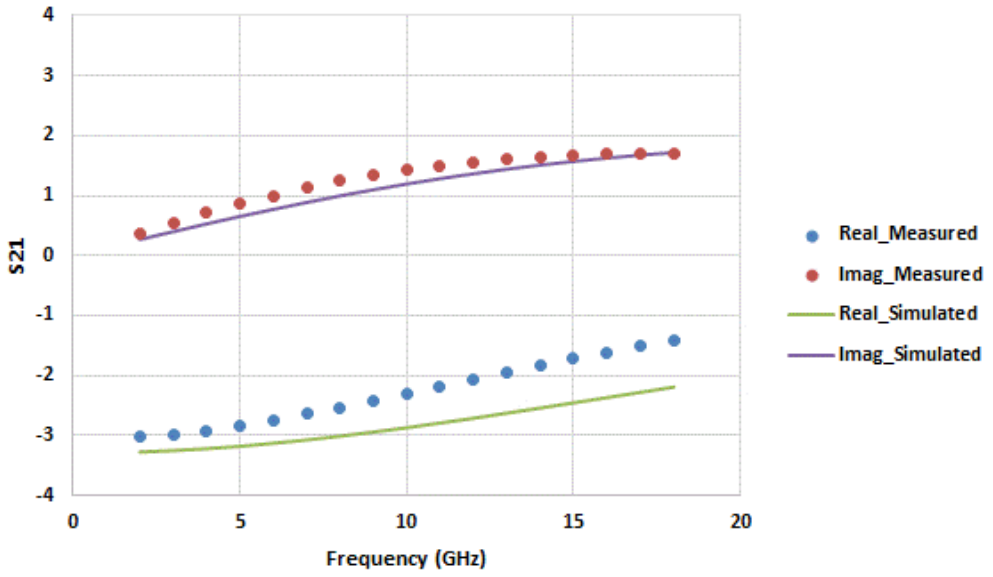

Figure 4.18. Measured vs simulated S21 for the sample SiGe HBT.

4.6.1 Noise Prediction over Temperature

Fig. 4.19 shows the comparison between the calculated NF_{min} and measured NF_{min} at the temperature from 25 ° C to 125 ° C. A good agreement has been obtained between the measured and calculated NF_{min} over an entire frequency range and over a wide temperature range. We find that the inclusion of the noise transit time τ_n and the correlation between the base and collector noise sources reduce the overall NF_{min} and its slope with frequency and temperature and improve the fit with the measurement. Also, we find that τ_n which is independent of frequency can give a good fit to the experiments.

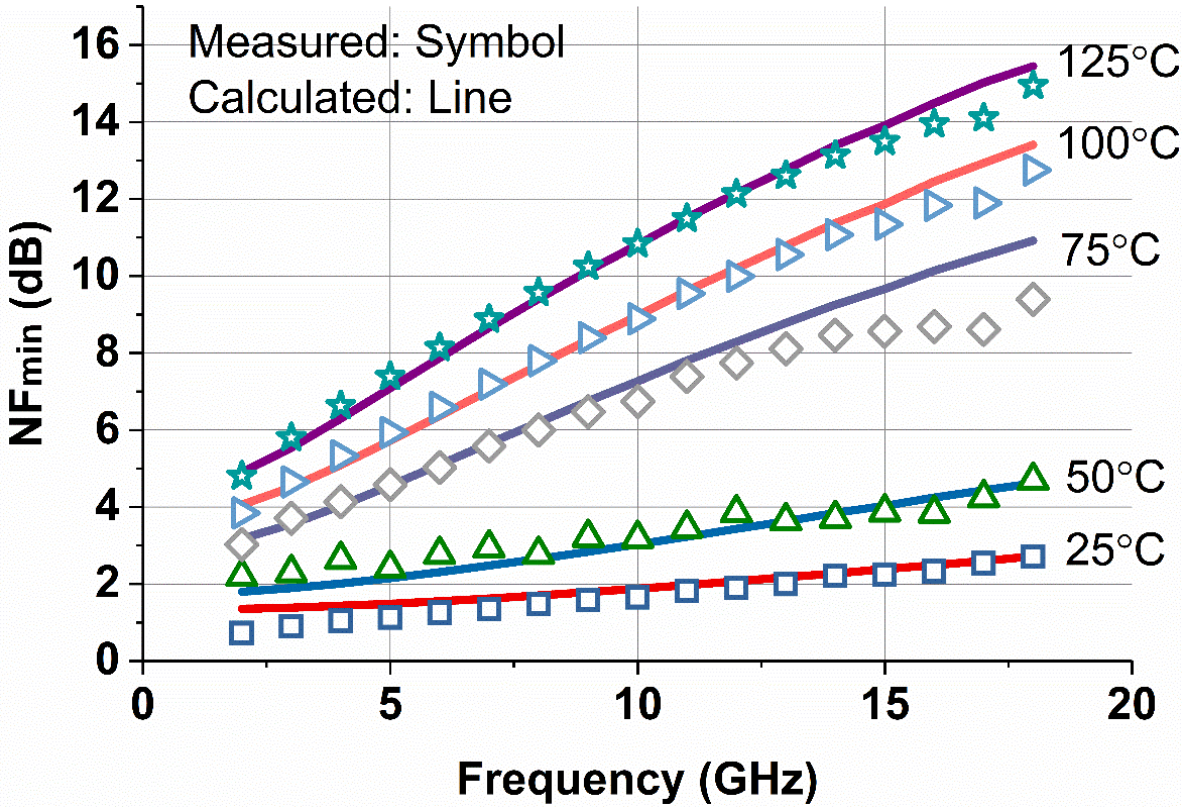

Figure 4.19. Sample SiGe HBT NF_{min} measured vs calculated with fitted noise transit time (τ_n) at $V_{be} = 0.9\ V$ and $V_{ce} = 1$ V. [28] © 2018, IEEE

The values of the best fitted noise ratio and the corresponding calculated NF_{min} at 10 GHz are used as references in Fig. 4.20 and Fig. 4.21, respectively.

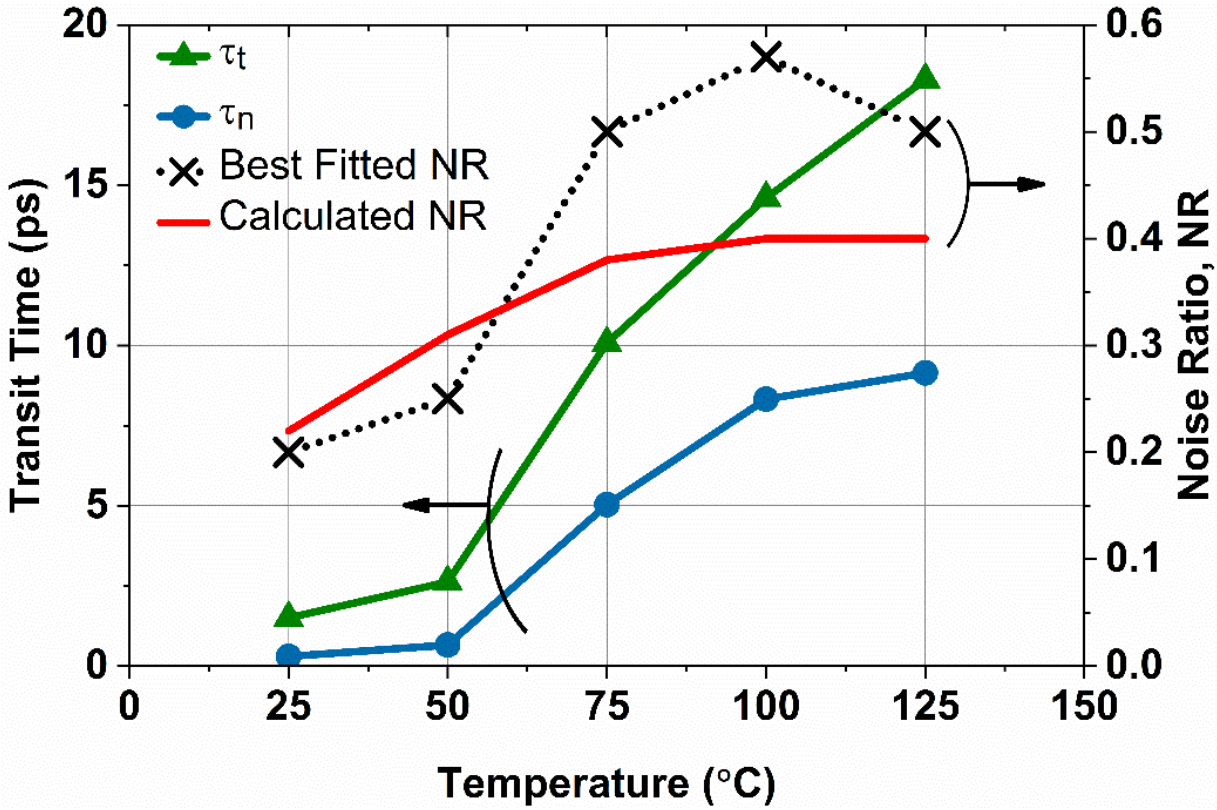

Figure 4.20. Temperature dependence of extracted vs fitted noise ratio, transistor transit time (τ_t) and noise transit time (τ_n) with $V_{be} = 0.9$ V and $V_{ce} = 1$ V. [28] © 2018, IEEE

Fig. 4.20 shows the temperature dependence of τ_t, τ_n and the noise ratio (NR). τ_t is extracted from the measured S-parameter data, and τ_n and the noise ratio (broken line) are the best fitted values from the tuner-based noise measurement. The noise ratio in solid line is calculated from the HICUM model. As the device goes into a high-current region at around 50 ° C, both τ_t and τ_n start to increase rapidly. Although the noise ratio calculated from the HICUM model

predicts its general behavior with temperature, the agreement with the fitted value is not very good, pointing to the difficulty in accurately calculating τ_n in the high-current region at high temperature.

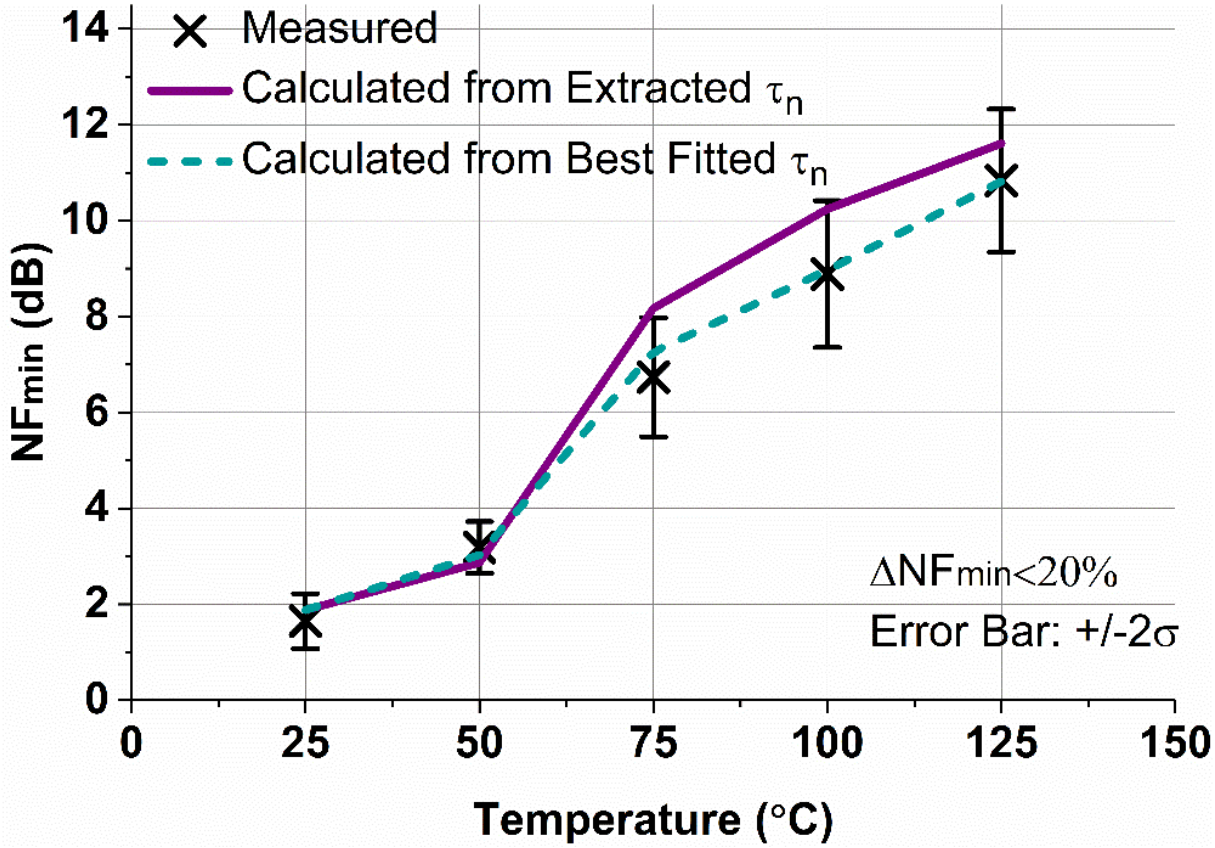

Figure 4.21. Temperature dependence of NF_{min} from measurement, calculation from fitted τ_n and extracted τ_n at 10 GHz with $V_{be} = 0.9$ V and $V_{ce} = 1$ V. [28] © 2018, IEEE

Fig. 4.21 shows the NF_{min} comparison over temperature for the tuner-based measurement, the calculation based on the best fitted noise transit time τ_n and the calculation based on the noise transit time τ_n from the HICUM model at 10 GHz. The error bars indicate +/-2σ uncertainty in the

measurement. The overall percentage error of the prediction of NF_{min} based on the calculated τ_n from the HICUM model is no more than 20% over temperature.

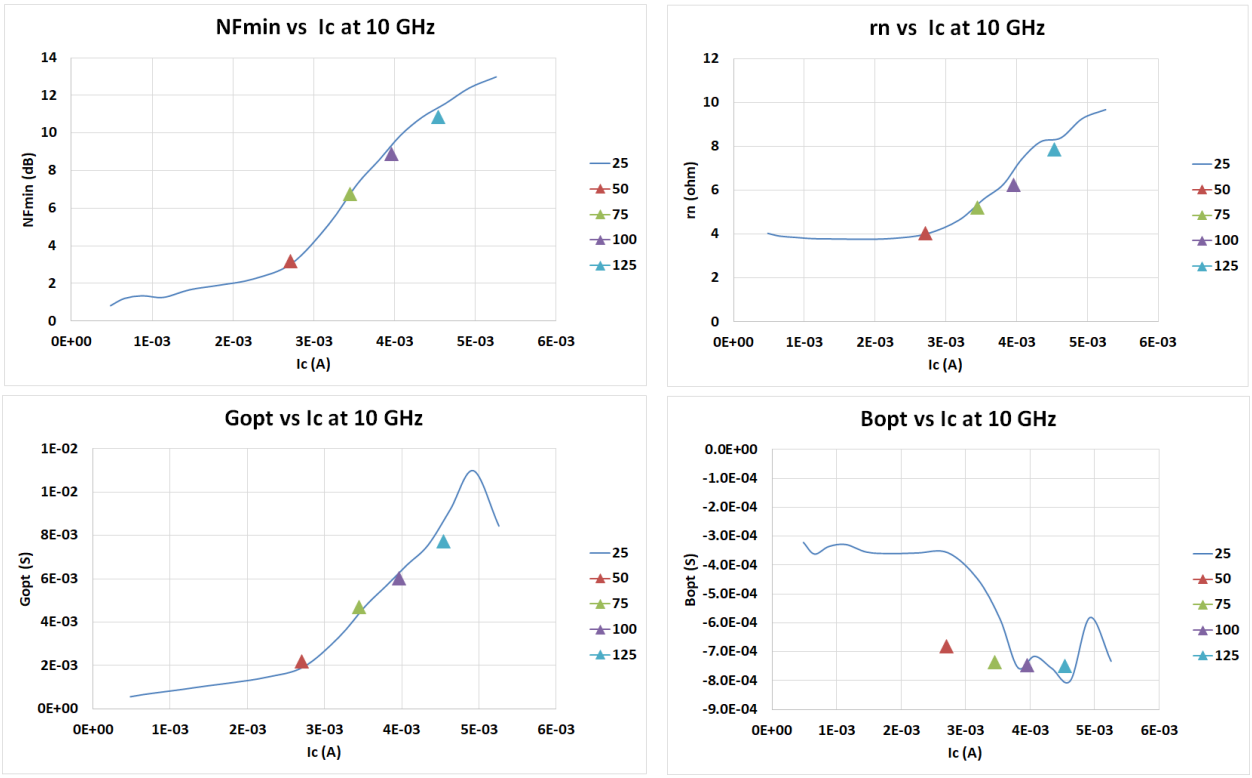

Figure 4.22. Collector current dependence of four noise parameters over temperature at 10 GHz with $V_{be} = 0.9$ V and $V_{ce} = 1$ V.

Fig. 4.22 shows the collector current dependence of four noise parameters from extracted τ_n over temperature at 10 GHz with $V_{be} = 0.9$ V and $V_{ce} = 1$ V. We find that the four noise parameters are only related with the bias collector current and the noise parameters of room temperature can predict the higher temperature data.

In order to clarify the relative contributions from the base resistance thermal noise ($4kTR_B$) and the correlated noise, Fig. 4.23 plots the contribution of the base resistance thermal noise and

the correlation term to the total noise power of the input noise voltage source in the chain representation ($\langle v_n^2 \rangle$ in Eqs. (2.33)-(2.35)) [9].

$$\langle v_n^2 \rangle = \langle v_{nB}^2 \rangle + \left|1 + \frac{Y_{22}}{Y_{21}}\right|^2 \langle v_{nE}^2 \rangle + \left|R_B + R_E\left[1 + \frac{Y_{22}}{Y_{21}}\right]\right|^2 \langle i_{nB}^2 \rangle + \left|Y_{21}^{-1} - R_E\left[1 + \frac{Y_{22}}{Y_{21}}\right]\right|^2 \langle i_{nC}^2 \rangle$$

$$- \frac{2}{|Y_{21}|^2} \Re\{(Y_{21}R_B + R_E[Y_{21} + Y_{22}]) \times (1 - R_E[Y_{21} + Y_{22}])^* \langle i_{nB} i_{nC}^* \rangle\}, \quad (4.37)$$

where $\langle v_{nB}^2 \rangle$ is the base thermal noise term and $\frac{2}{|Y_{21}|^2} \Re\{(Y_{21}R_B + R_E[Y_{21} + Y_{22}]) \times (1 - R_E[Y_{21} + Y_{22}])^* \langle i_{nB} i_{nC}^* \rangle\}$ is the correlation term.

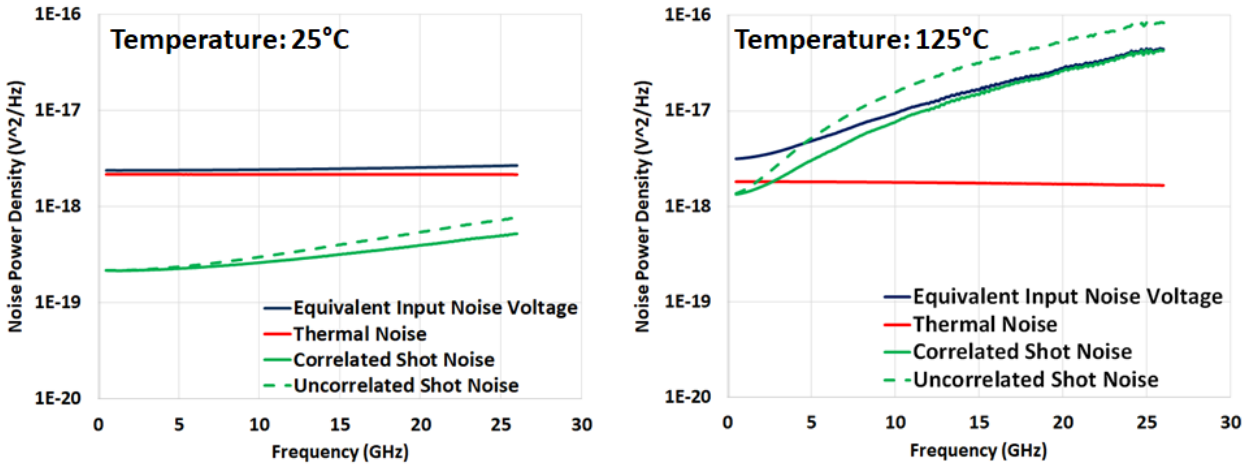

Figure 4.23. Plots showing the relative contributions of the base resistance thermal noise and the noise correlation to the total noise of the input referred noise voltage in the chain representation at 25 °C and 125 °C.

The correlation effect is smaller than the base resistance thermal noise at 25 °C, but the situation is reversed at 125 °C. The rapid increase of the correlation effect from 25 °C to 125 °C is due to the increase in τ_n as shown in Fig. 4.20. Please note that the base resistance thermal noise

at 125 °C is actually lower than at 25 °C because the base resistance value is lower at 125 °C. The reason is that with the biasing of $V_{be} = 0.9$ V, the base current at 125 °C is much higher than at 25 °C which causes the base resistance to decrease due to the conductivity modulation. This more than offsets the slight increase of the external base sheet resistance at 125 °C. Please note also that the figure plots only the input voltage noise power $\langle v_n^2 \rangle$. The input current noise power ($\langle i_n^2 \rangle$, which is not shown) does not have the contribution from the base resistance thermal noise.

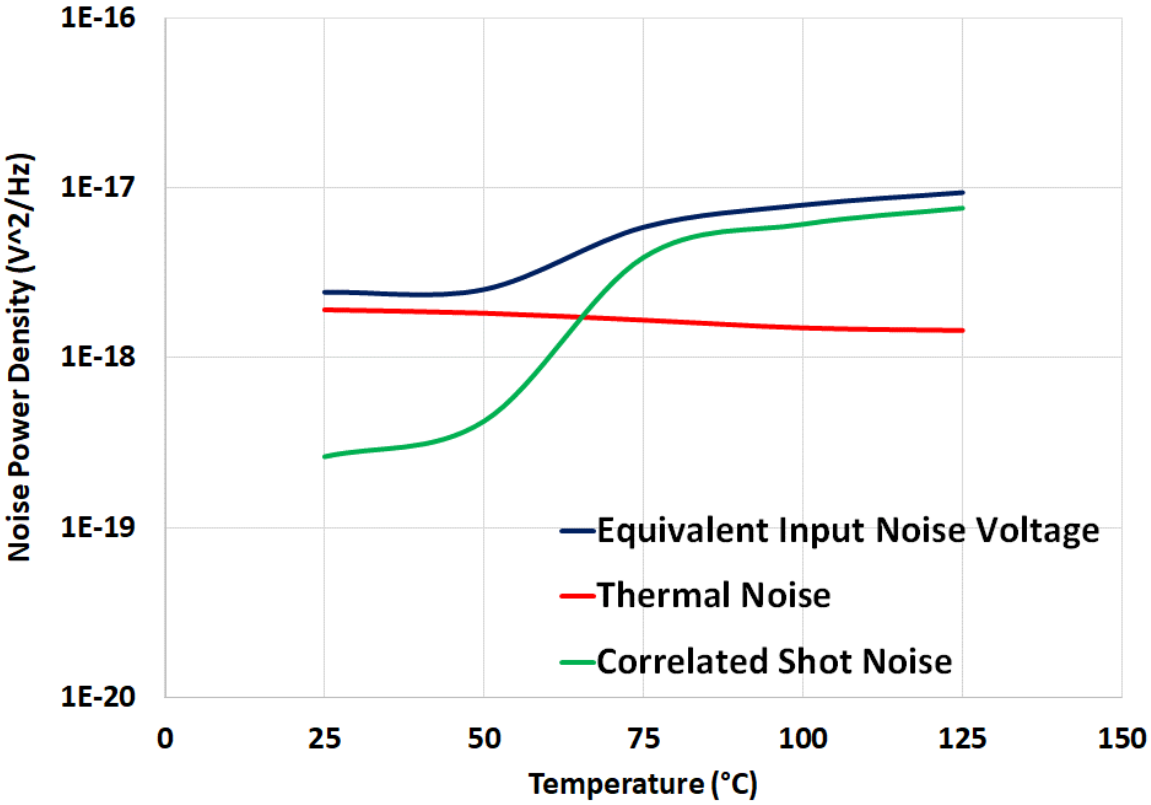

Figure 4.24. Temperature dependence of contributions of the base resistance thermal noise and the noise correlation to the total noise of the input referred noise voltage in the chain representation at 10 GHz.

Fig. 4.24 shows the temperature dependence of noise contributions of the input referred noise voltage at 10 GHz. We can find that the noise contribution of correlated shot noise sharply increases and becomes the dominant component when the device's temperature gets above 65 °C.

4.6.2 Noise Prediction over Bias Current

Next, we present the prediction results over bias current based on the same SiGe HBT transistor.

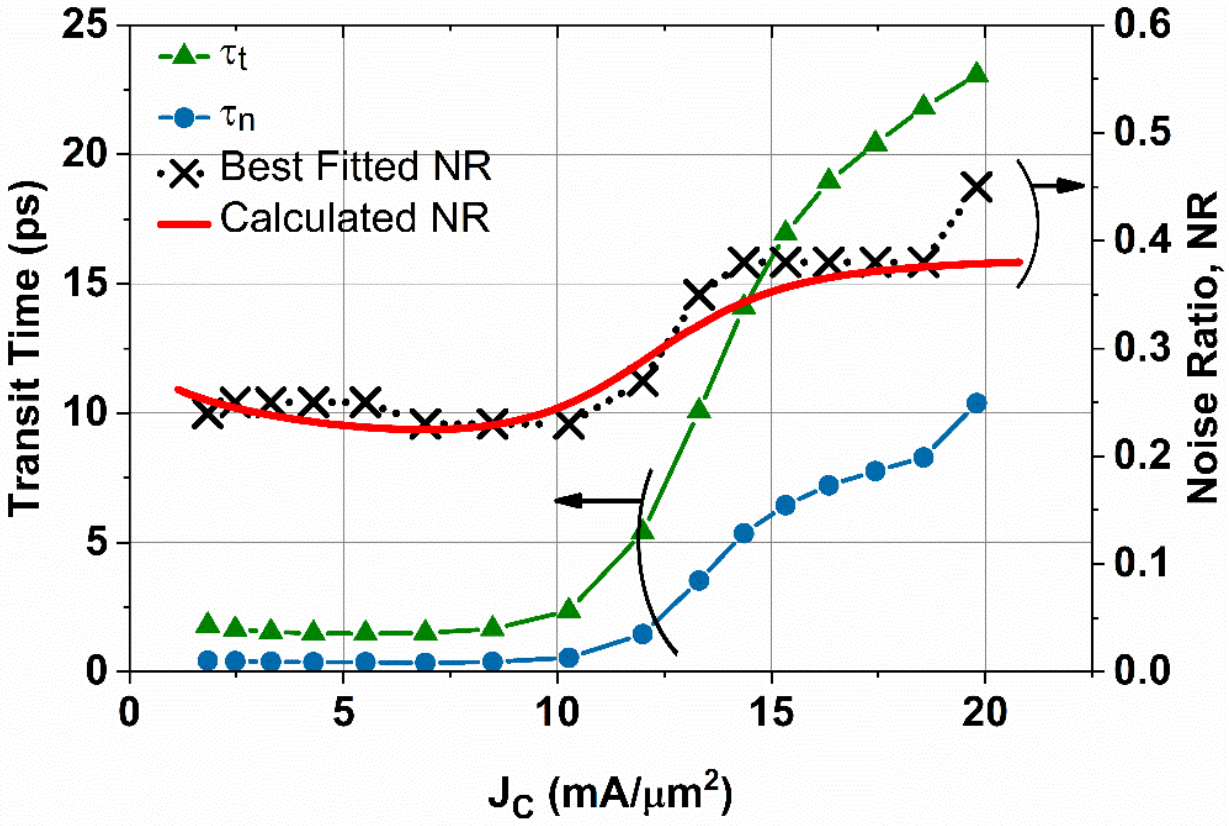

Figure 4.25. Bias current dependence of extracted vs fitted noise ratio, transistor transit time (τ_t) and noise transit time (τ_n) with $V_{ce} = 1$ V at 25 °C. [28] © 2018, IEEE

Fig. 4.25 shows the bias current dependence of τ_t, τ_n and the noise ratio (NR) at room temperature. A good agreement is obtained between the noise ratio calculated from the HICUM model (solid line) and the best fitted results from the measurement (symbol x), which validates the extracted τ_n from the HICUM model. The agreement is much better than the case for the temperature dependence (Fig. 4.20).

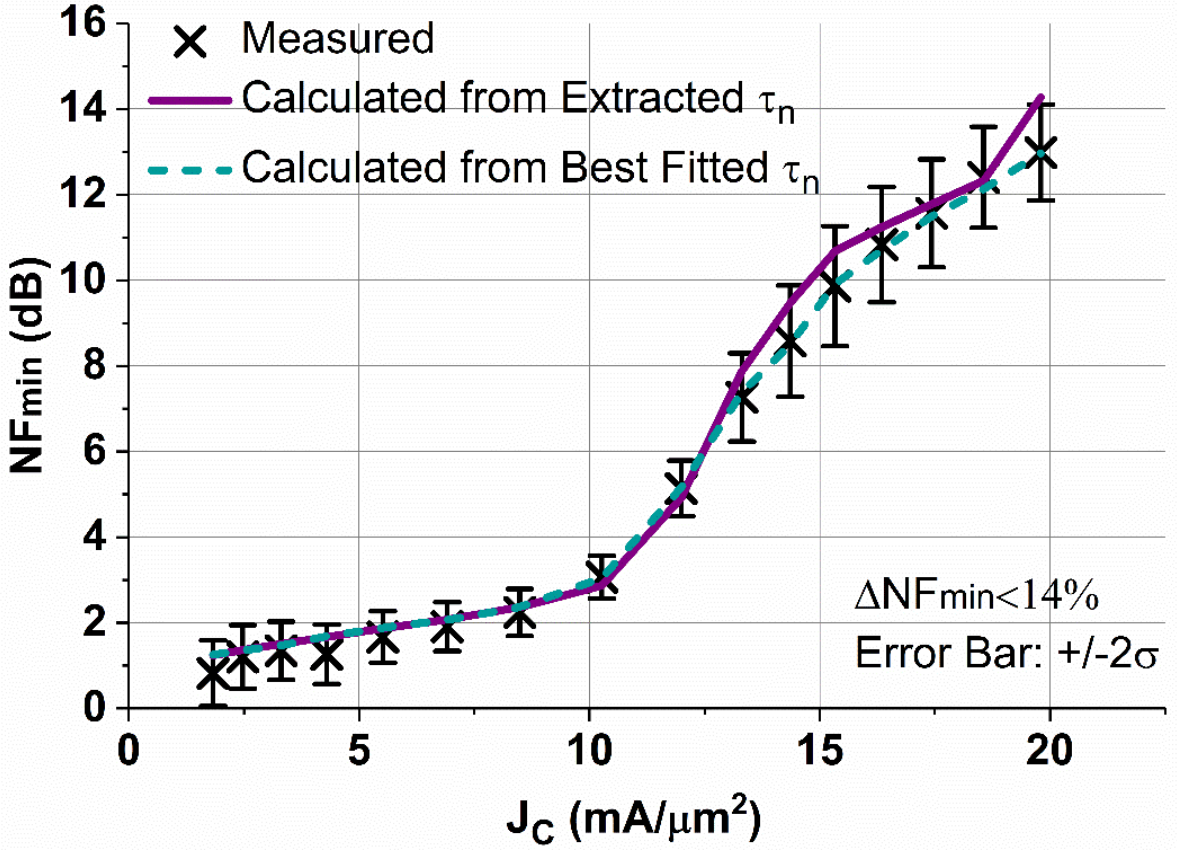

Figure 4.26. SiGe HBT bias current dependence of measured vs calculated noise ratio with V_{ce} = 1 V at 10 GHz at 25 °C. [28] © 2018, IEEE

Fig. 4.26 shows the comparison of bias current dependence of NF_{min} at 10 GHz between the tuner-based measurement and the Y-parameter calculation based on the best fitted τ_n. Good

agreement has been obtained over the entire frequency range (2GHz to 18GHz) and over bias. At J_c of around 12 mA/μm^2, the device goes into a high-injection region, and the noise ratio again increases. The overall percentage error of the prediction of NF_{min} based on the calculated τ_n from the HICUM model is no more than 14% over the bias.

We now discuss the validation of bias dependence of the noise parameters. Fig. 4.27 shows the r_n, G_{opt} and B_{opt} comparison between the measurement and calculation from the fitted and extracted τ_n over bias at 10 GHz at room temperature. Similarly to NF_{min} shown in Fig. 4.26, r_n, G_{opt} and B_{opt} all have good agreement between the calculated and measured results. The deviation in B_{opt} is larger than the other parameters, and is most likely caused by an uncertainty in the emitter resistance value.

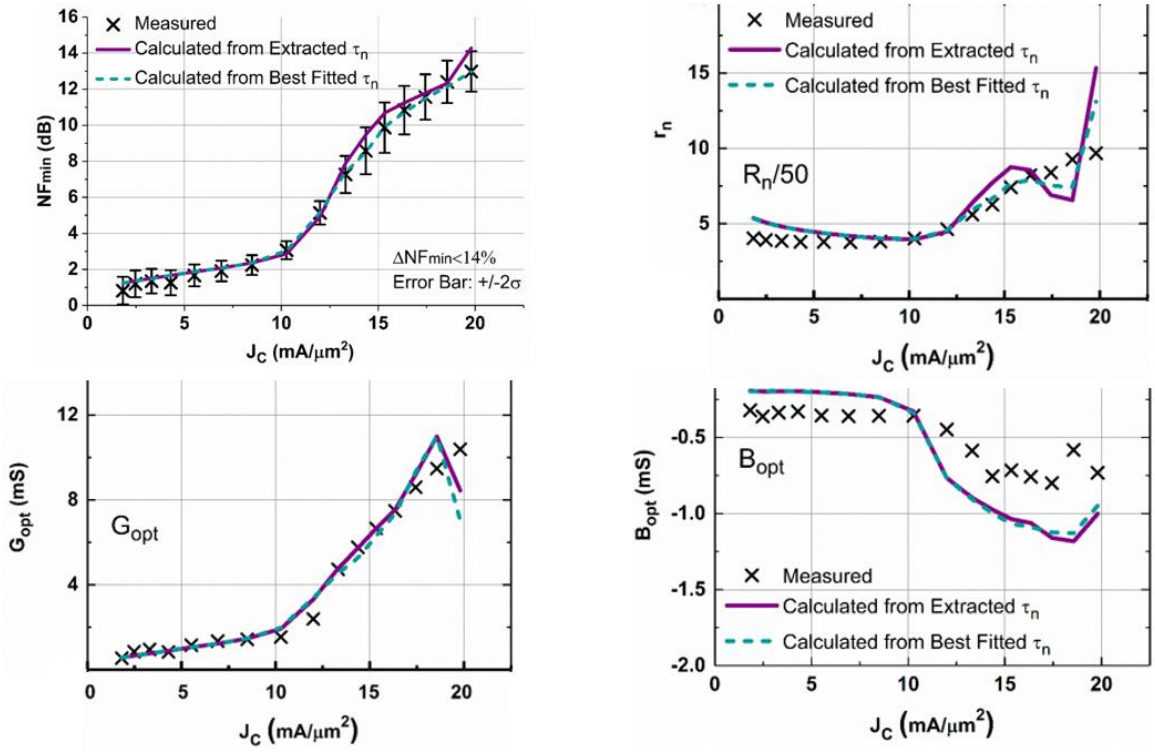

Figure 4.27. Bias dependence of four noise parameters from measurement, calculation from fitted τ_n and extracted τ_n at 10 GHz with $V_{ce} = 1$ V at 25 ° C. [28] © 2018, IEEE

4.6.3 Noise Prediction over Frequency

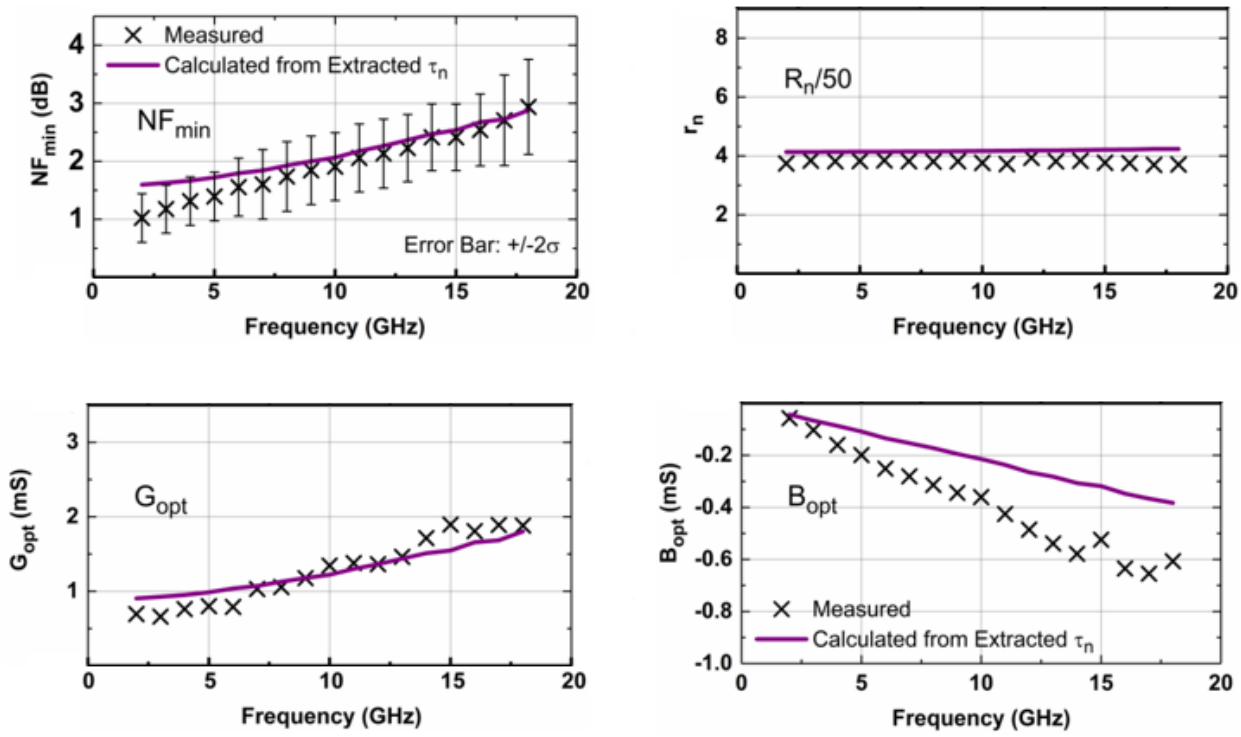

Figure 4.28. Comparison of four noise parameters between measurement (solid) and calculation (dotted) based on τ_n from HICUM model with $V_{be} = 0.9$ V and $V_{ce} = 1$ V at room temperature. [28] © 2018, IEEE

Fig. 4.28 shows a good agreement of the four noise parameters between the calculation from the HICUM model and the results from the tuner-based measurement over frequency. From the figure, we find that NF_{min} increases with frequency, the normalized equivalent noise resistance ($r_n = R_n/50$) is constant with frequency, the real part of the optimum source admittance (G_{opt}) increases with frequency and the imaginary part of the optimum source admittance (B_{opt}) decreases with frequency.

Again, the discrepancy between the calculated and measured B_{opt} comes from the R_E extraction deviation. Fig. 4.29 shows the R_E dependence of extracted optimum source susceptance (B_{opt}) over frequency. B_{opt} gets a better fits by reducing the value to 1/2 of the extracted. Since the R_E value we used gives good fit to the rest of the parameters, we did not readjust its value. It is difficult to use one value to fit all the parameters.

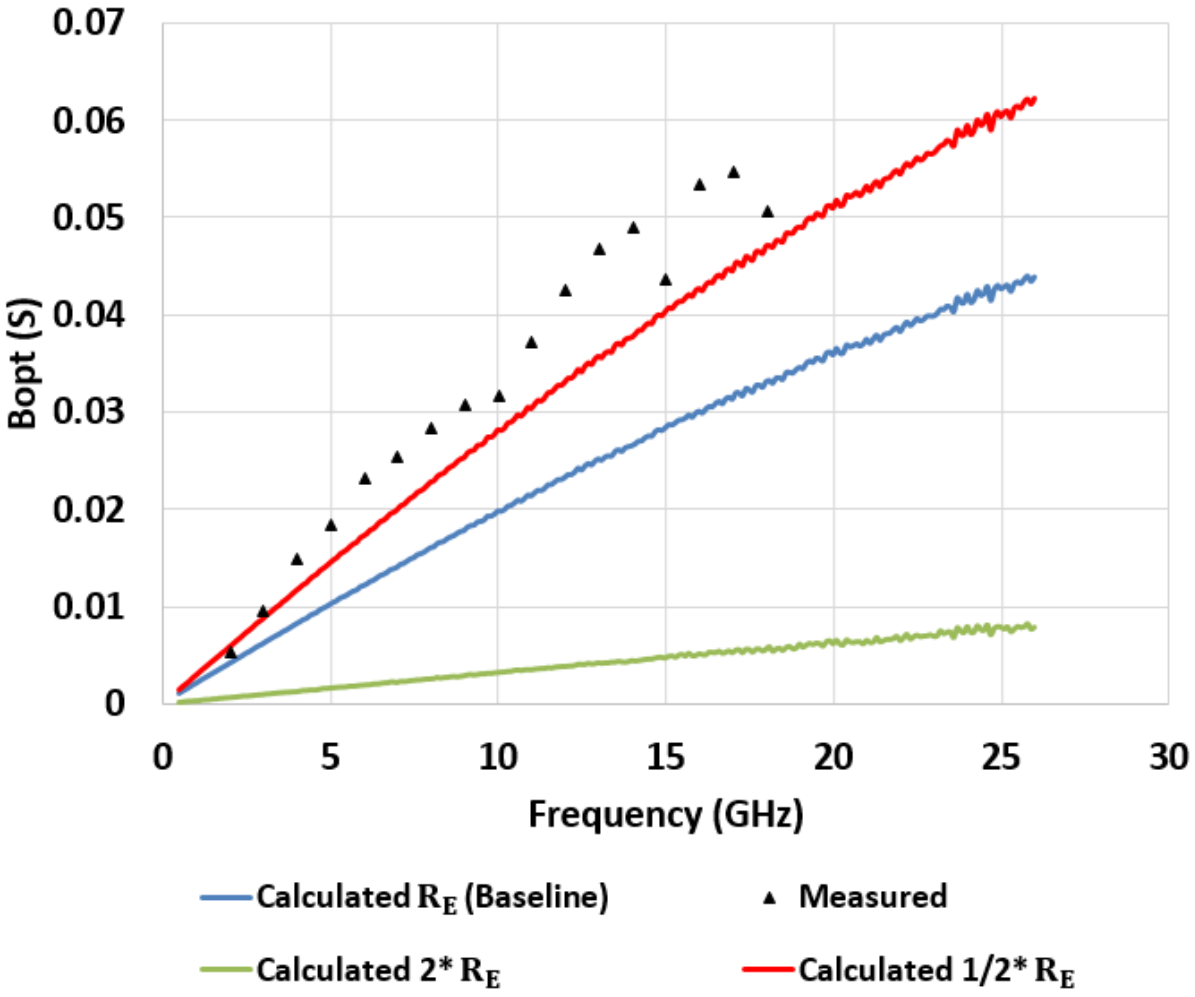

Figure 4.29. R_E dependence of extracted optimum source susceptance (B_{opt}) over frequency.

4.6.4 Noise Prediction over Transistor Size

We now discuss the validation of the prediction method over size. The SiGe HBT devices we used have the same emitter length but emitter width varies from 0.28 μm to 0.42 μm. Fig. 4.30 shows the NF_{min} over bias for both devices.

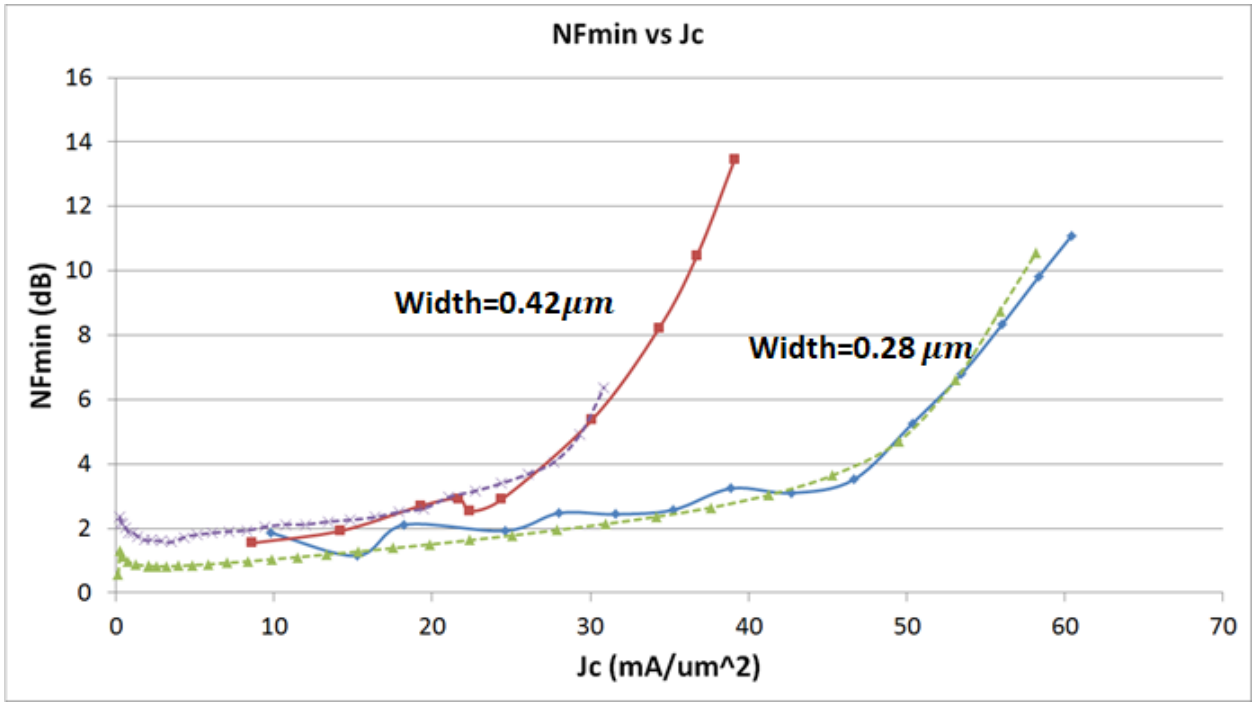

Figure 4.30. Size dependence of measured (solid) and calculated (dotted) NF_{min} over collector current density J_c.

Excellent agreement is achieved between the measured and calculated NF_{min} for both 0.28μm and 0.42μm width devices over collector current density. We find that the smaller emitter width device has a lower noise figure at the same collector current density, because a smaller base resistance for the smaller width device directly translates into a smaller NF_{min}.

4.6.5 Noise Prediction over Technology Scaling

We now discuss the validation of the prediction method over technology scaling. The device used for the measurement and calculation were fabricated with a more advanced technology with the f_T up to 220 GHz. As shown in Fig. 4.31, the calculation method works well for predicting the full noise properties over bias current.

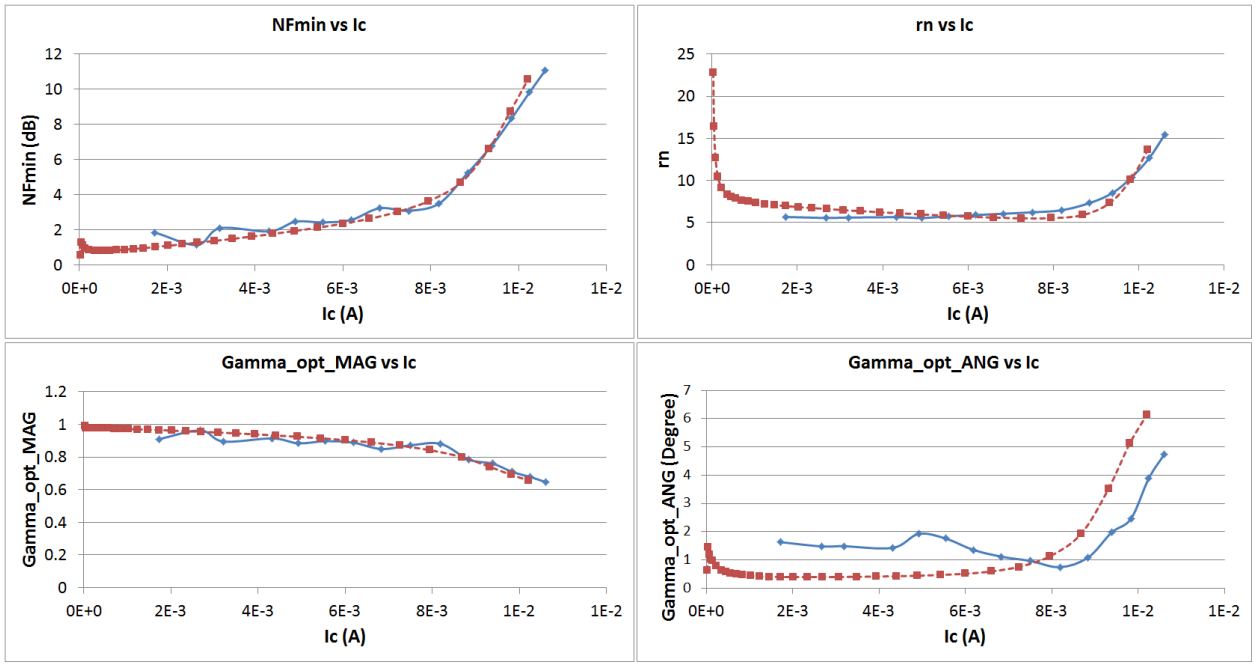

Figure 4.31. Technology scaling dependence of measured (solid) and calculated (dotted) four noise parameters over bias current.

4.7 Comparison with HICUM Noise Model

In HICUM noise model, the correlation between base and collector noise is also discussed. According to the model manual [25], the correlation term is given by

$$\langle i_{nB}^{*} i_{nC} \rangle = 2qI_c j\omega\tau_{Bf}\alpha_{it} \cdot \Delta f \,, \tag{4.38}$$

where τ_{Bf} is base transit time and α_{it} is the correlation factor with a default constant value (1/3).

The collector shot noise is given by

$$\langle i_{nC}^2 \rangle = 2qI_C \cdot \Delta f \ . \tag{4.39}$$

The base current related noise spectral density is

$$\langle i_{nB}^2 \rangle = 2qI_{jBEi}\left[1 + 2\alpha_{qf}B_f\left(\omega\tau_{Bf}\right)^2\right] \cdot \Delta f \ . \tag{4.40}$$

This can be compared with the transport model

$$\langle i_{nB}^2 \rangle = [2qI_b + 4qI_c\left(1 - \Re\left\{e^{-j\omega\tau_n}\right\}\right)] \cdot \Delta f \tag{4.41}$$

$$\langle i_{nC}^2 \rangle = 2qI_c \cdot \Delta f \tag{4.42}$$

$$\langle i_{nB}^* i_{nC} \rangle = 2qI_c\left(e^{-j\omega\tau_n} - 1\right) \cdot \Delta f \ . \tag{4.43}$$

The HICUM noise model includes only the effect of base transit time, and not the delay time due to the CB space-charge region.

According to the HICUM manual α_{it} is a constant value, but based on our measurement results α_{it} should be dependent on temperature and bias.

4.8 Conclusion

In this chapter, we discussed the origin and the impact of the noise transit time on the noise correlation. Then, we proposed the method to extract the noise transit time from HICUM model. Also, this chapter demonstrated the extraction of base and emitter resistances and the completed procedure for noise calculation with a sample SiGe HBT transistor.

CHAPTER 5

NOISE CALCULATION OF MOSFETS

5.1 Noise Sources in MOSFETs

This section discusses the high frequency noise of MOSFET devices for the channel length from 130 nm to 40 nm. For MOSFET devices, thermal noise is the dominant component at high frequency range. The equivalent noise model of MOSFET devices can be treated as a modulated resistor and the channel noise coupling to the gate through the gate capacitance. Van der Ziel [36] has proposed a thermal noise model for MOSFET device, which includes the drain current noise, induced gate current noise and their cross-correlation coefficient as follows [36]

$$S_{id} = 4kT\gamma g_{ds0} \tag{5.1}$$

$$S_{ig} = 4kT\delta g_g \tag{5.2}$$

$$S_{i_d^* i_g} = c\sqrt{\langle i_d^2\rangle\langle i_g^2\rangle} \tag{5.3}$$

$$g_g = \zeta\frac{\omega^2 C_{gs}^2}{g_{ds0}}, \tag{5.4}$$

where γ is the excess noise factor which explains the microscopic excess noise effect, g_{ds0} is the output conductance given by $\frac{\partial I_D}{\partial V_{DS}}$ at $V_{DS} = 0$, g_g is the real part of the gate-to-source admittance and c is the cross-correlation coefficient.

For short channel devices, the effect from the gate resistance is even important. The thermal noise voltage generated by the gate resistance can be transferred to the drain current via g_m [37]

$$\Delta S_{id} = 4kTR_g {g_m}^2 . \tag{5.5}$$

At the same time, gate resistance impacts the induced gate noise as

$$S_{ig} = 4kTR_g\omega^2 C_{gg}^2 , \tag{5.6}$$

where C_{gg} is the total gate capacitance.

For a sample 130 nm NMOS device, the drain current noise, gate resistance induced drain current noise and the gate resistance induced gate noise have been calculated and plotted in Fig. 5.1. The extracted small-signal parameters of the sample device are listed in Table 5.1.

Table 5.1. Extracted small-signal parameters of a sample 130 nm MOSFET.

R_g	g_m	g_{ds0}	C_{gs}
4 ohm	0.046 S	0.108 S	4.6e-14 F

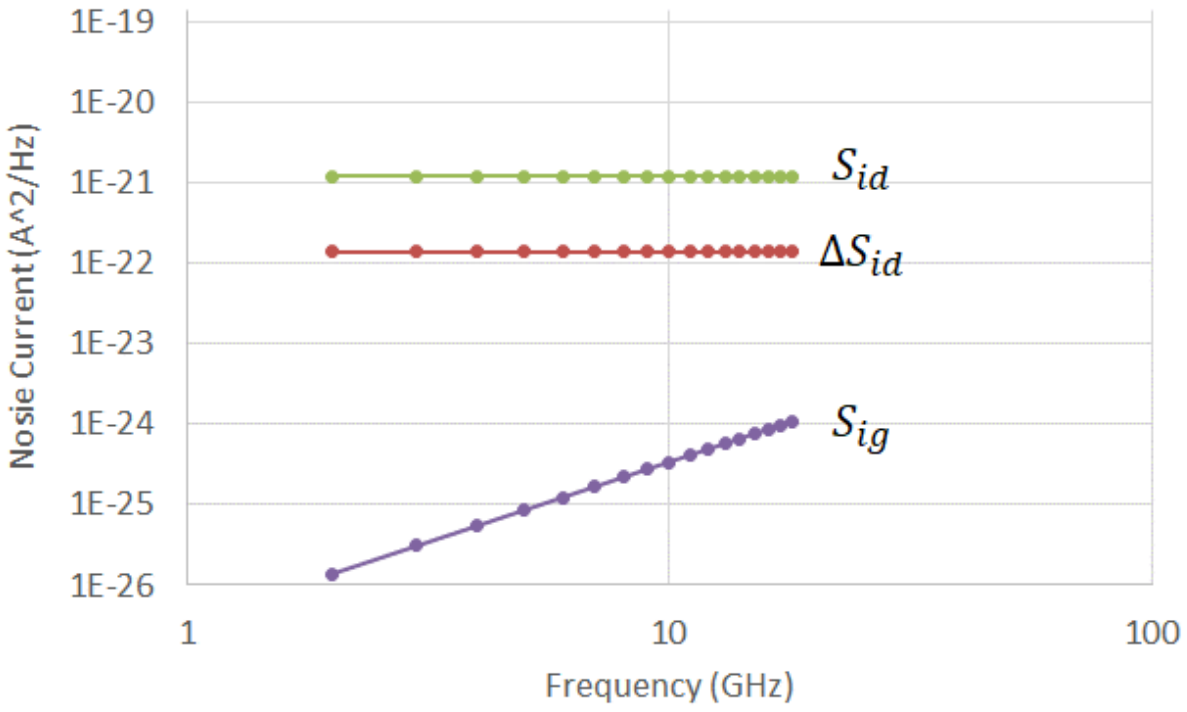

Figure 5.1. Calculated noise sources of a sample 130 nm MOSFET transistor.

From Fig. 5.1, we find that gate resistance induced gate noise can be ignored in this frequency range compared with drain current noise and gate resistance induced drain current noise. To evaluate the excess noise factor γ, we first review the BSIM model. Based on the equations in [38], we simulate the excess noise factor for long-channel ($3\mu m$) device and obtain the well-known limiting values [38] as shown in Fig. 5.2:

1. $\gamma = 1$ in the linear region.
2. $\gamma \approx 2/3$ in saturation above threshold.
3. $\gamma = 0.5$ in saturation below threshold.

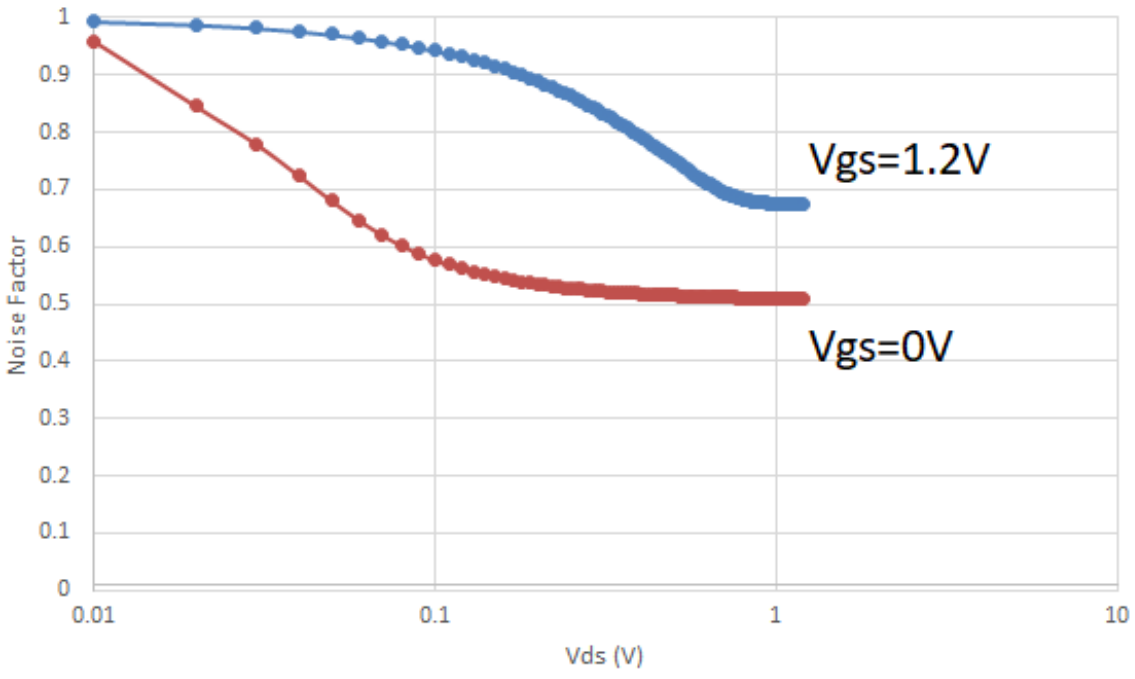

Figure 5.2. Simulated excess noise factor for long-channel device ($3\mu m$).

5.2 Noise Calculation for MOSFETs

As the MOSFET channel length is scaling down to sub-100nm, two effects increase the excess noise factor above 2/3 in saturation region above threshold: channel-length modulation and more significantly resistance effects [37]. Therefore, we will introduce a method to calculate the excess noise factor based on Y-parameter and tuner-based noise measurement.

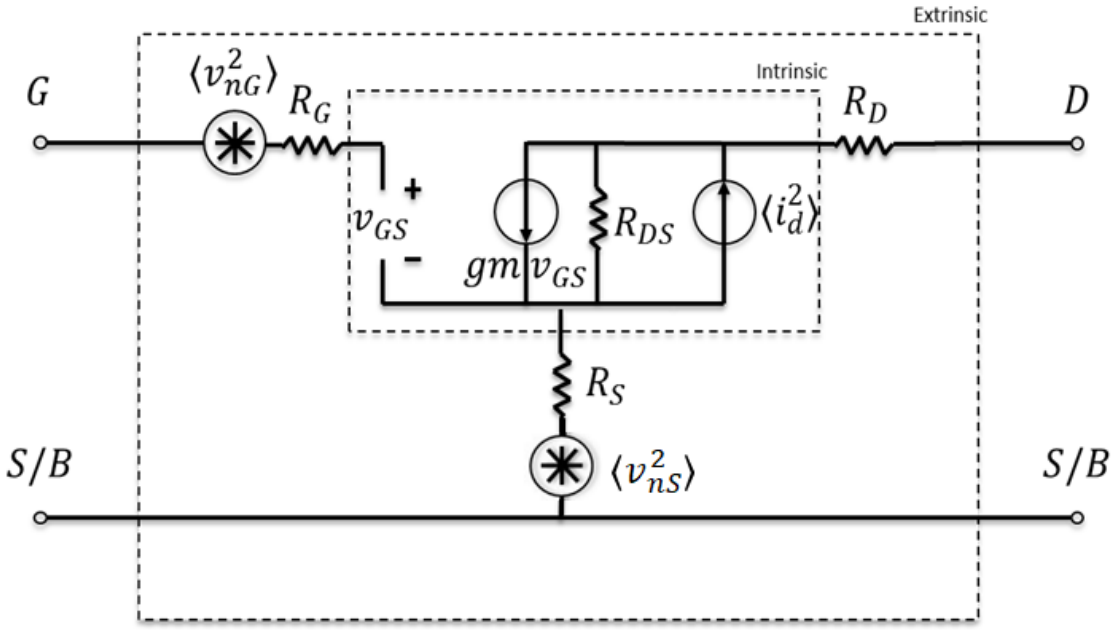

Figure 5.3. Y-parameter equivalent circuit for MOSFETs.

Similarly to the SiGe HBT case, the internal noise sources shown in Fig. 5.3 can be transferred to the input of the transistor as noise voltage source (v_n^2) and noise current source (i_n^2) by calculating from the measured Y-parameters [9]. The equivalent input voltage source and input current source can be given by

$$\langle v_n^2 \rangle = \langle v_{nG}^2 \rangle + \left|1 + \frac{Y_{22}}{Y_{21}}\right|^2 \langle v_{nS}^2 \rangle + \left|Y_{21}^{-1} - R_S[1 + \frac{Y_{22}}{Y_{21}}]\right|^2 \langle i_d^2 \rangle \tag{5.7}$$

$$\langle i_n^2 \rangle = \left| \frac{Y_{11} - R_S \det[Y]}{Y_{21}} \right|^2 \langle i_d^2 \rangle + \left| \frac{\det[Y]}{Y_{21}} \right|^2 \langle v_{nS}^2 \rangle \tag{5.8}$$

$$\langle v_n^* i_n \rangle = \frac{\det[Y]}{Y_{21}} (1 + \frac{Y_{22}}{Y_{21}})^* \langle v_{nS}^2 \rangle + \left(\frac{Y_{11} - R_S \det[Y]}{Y_{21}} \right) \left(Y_{21}^{-1} - R_S \left[1 + \frac{Y_{22}}{Y_{21}} \right] \right)^* \langle i_d^2 \rangle , \tag{5.9}$$

where $[Y]$ is the measured Y-parameters of the NMOS after the OPEN&SHORT pads de-embedding. Therefore, the four noise parameters can be represented by the equivalent input noise sources based on the equations in [8]

$$R_n = \frac{\langle v_n^2 \rangle}{4kT} \tag{5.10}$$

$$Y_{opt} = \sqrt{\frac{\langle i_n^2 \rangle}{\langle v_n^2 \rangle} - \left[\Im \left(\frac{\langle v_n i_n^* \rangle}{\langle v_n^2 \rangle} \right) \right]^2} + j \Im \left(\frac{\langle v_n i_n^* \rangle}{\langle v_n^2 \rangle} \right) \tag{5.11}$$

$$F_{min} = 1 + \frac{\langle v_n i_n^* \rangle + \langle v_n^2 \rangle Y_{opt}^*}{2kT}, \tag{5.12}$$

where k is the Boltzmann constant and T is the absolute temperature.

Based on the equations (5.7) and (5.10), the drain noise current can be derived as

$$\langle i_d^2 \rangle = \frac{4kTR_n - \langle v_{nG}^2 \rangle - \left| 1 + \frac{Y_{22}}{Y_{21}} \right|^2 \langle v_{nS}^2 \rangle}{\left| Y_{21}^{-1} - R_S [1 + \frac{Y_{22}}{Y_{21}}] \right|^2}. \tag{5.13}$$

At the same time, based on the definition of γ, we have

$$\gamma = \frac{\langle i_d^2 \rangle}{4kT g_{ds0}}. \tag{5.14}$$

Therefore, the excess noise factor γ can be calculated from the measured four noise parameters based on the procedure we discussed in this section. In the following section, we will discuss the experimental results of a sample NMOS transistor.

The gate, source and drain resistances can be extracted from the measured S-parameter data at $V_{ds} = 0$ by [39]

$$R_g = \left|\frac{\Re(Y_{12})}{\Im(Y_{12})\Im(Y_{11})}\right| \tag{5.15}$$

$$R_d = \left|\frac{\Re(Y_{21}) - \Re(Y_{12})}{\Im(Y_{12})^2}\right| \tag{5.16}$$

$$R_s = \left|\frac{\Re(Y_{11})}{\Im(Y_{11})^2} - R_g - \frac{C_{gd}^2}{C_{gg}^2}R_d\right| * \frac{C_{gg}^2}{C_{gs}^2}. \tag{5.17}$$

The extracted gate, source and drain resistances of the sample 130 nm MOSFET device are shown in Fig. 5.4.

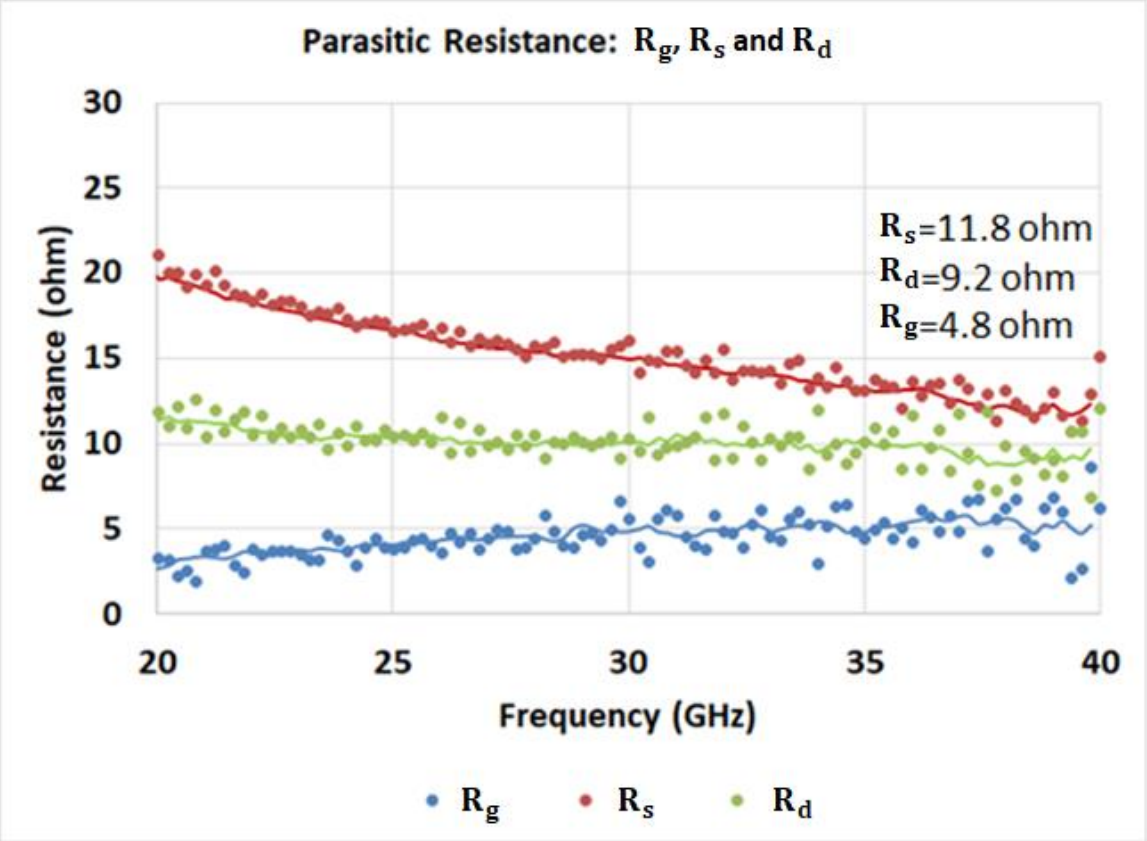

Figure 5.4. Extracted gate, source and drain resistances of the sample 130 nm MOSFET.

In Fig. 5.5, the extracted excess factor γ is calculated for both 40 nm and 130 nm MOSFET devices. We find that the excess noise factor for 40 nm MOSFET is much higher than 130 nm which is also observed in [37], but the values are considerably higher than [37].

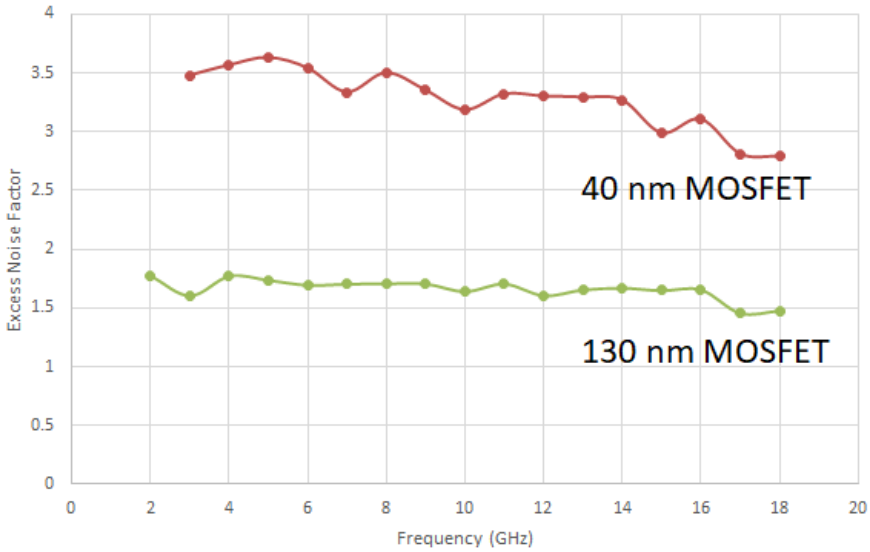

Figure 5.5. Extracted excess noise factor.

In Fig. 5.6 and Fig. 5.7, the V_{gs} and V_{ds} dependences of γ are calculated based on the Y-parameter and tuner-based measurement results.

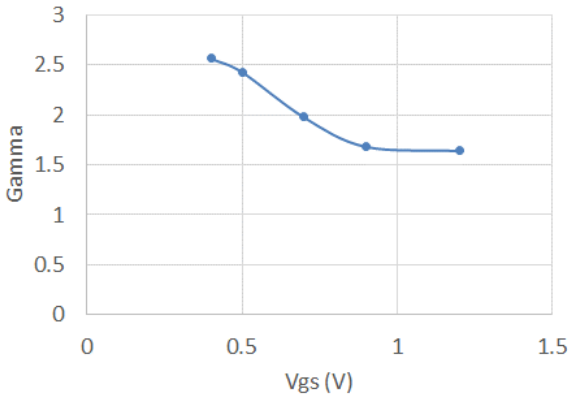

Figure 5.6. Calculated γ versus V_{gs} bias at 10 GHz and $V_{ds} = 1.2V$ for 130 nm MOSFET.

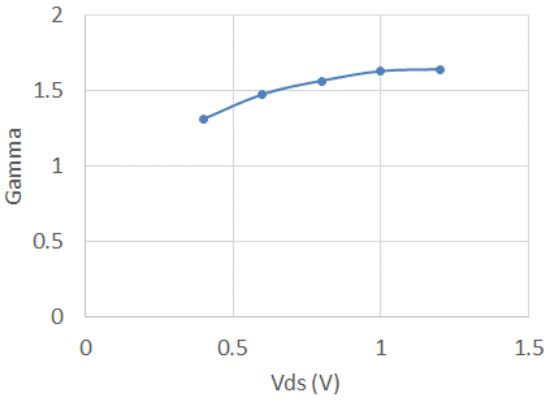

Figure 5.7. Calculated γ versus V_{ds} bias at 10 GHz and $V_{gs} = 1.2V$ for 130 nm MOSFET.

5.3 Noise Model Validation of MOSFETs

Then the calculated NF_{min} is validated over the frequency. A good agreement is achieved between the calculated and measured NF_{min} as shown in Fig. 5.8.

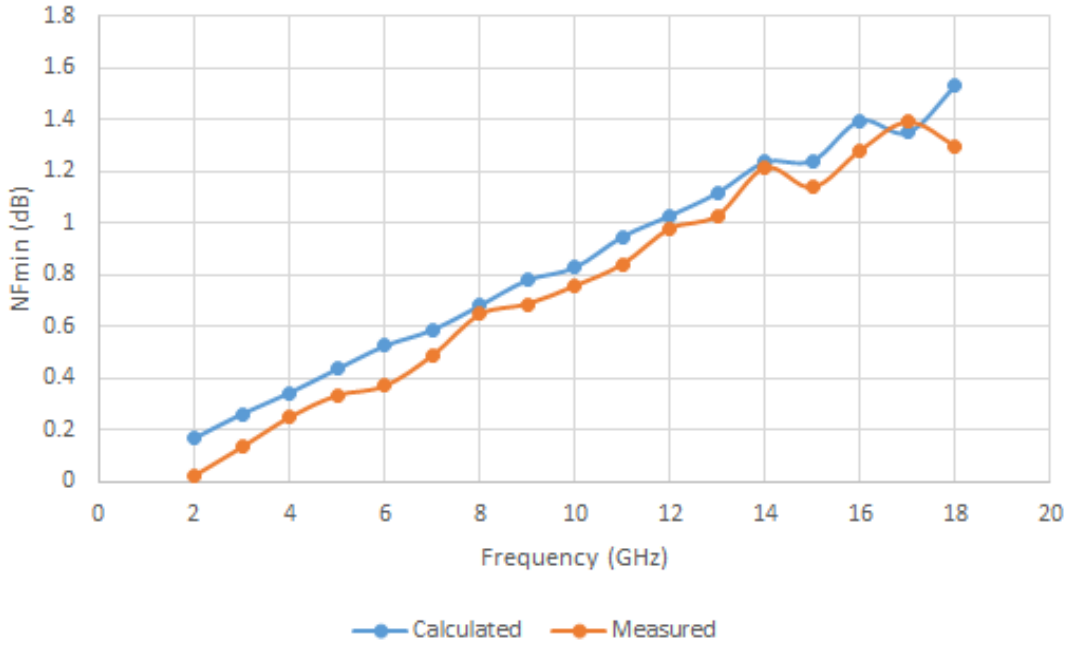

Figure 5.8. Measured vs calculated NF_{min} over frequency for 130 nm MOSFET.

For the MOSFET devices, we characterized the high frequency noise of a sample 130 nm MOSFET transistor over the temperature and frequency up to 18 GHz. The measurement results are compared with the calculation results based on the noise model we discussed in Section 5.2. The excess noise factor can be obtained by fitting the calculated NF_{min} from the tuner-based noise measurement.

Fig. 5.9 shows the temperature dependence of NF_{min} comparison between the tuner-based measurement and the Y-parameter calculation based on the best fitted γ. As shown in the figure,

both the value and slope of NF_{min} are increasing with the temperature. A good agreement has been obtained between the calculation and measurement over the temperature and frequency.

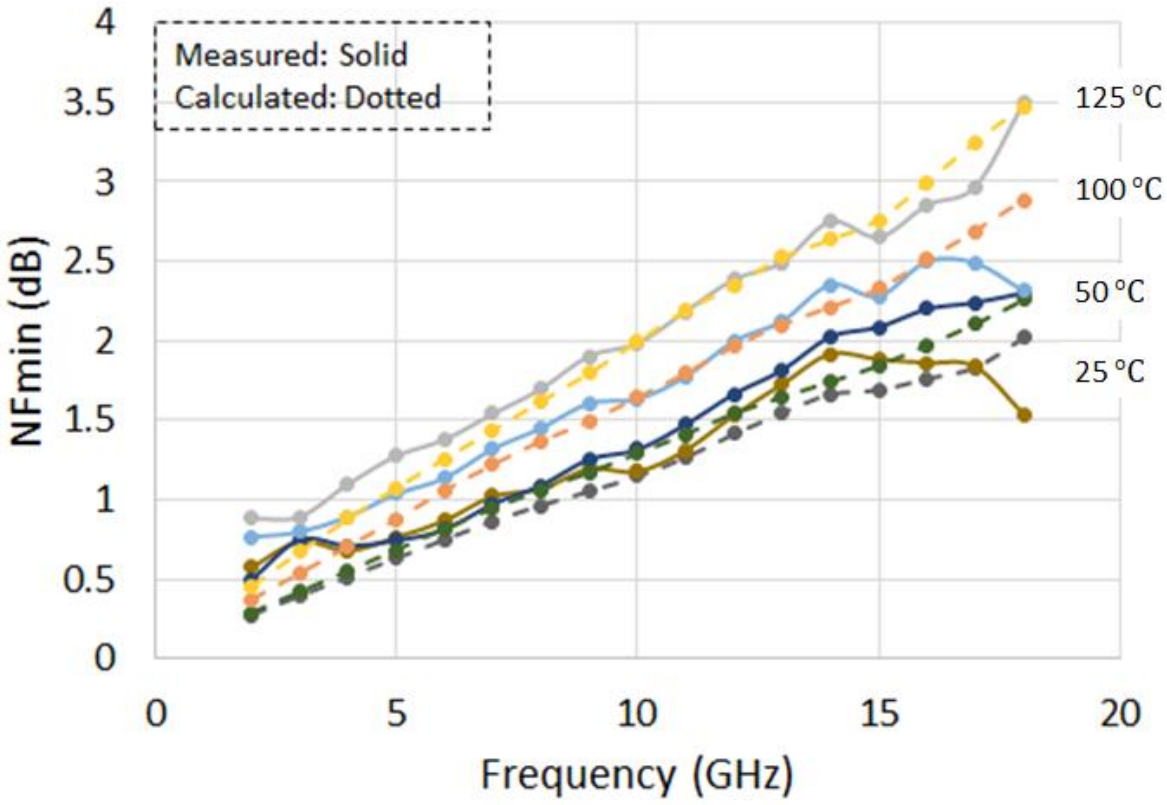

Figure 5.9. Sample 130 nm NMOS NF_{min} measured vs calculated with fitted excess noise factor γ at $V_{gs} = 1.2V$ and $V_{ds} = 1.2V$.

Now, we will analyze the γ over temperature. Fig. 5.10 shows the temperature dependence of NF_{min} comparison between measurement and calculation and the fitted excess noise factor γ at 10 GHz. We find that the γ is keeping constant at the temperature below 50 °C and sharply increasing at higher temperature. This result can be a reference for the development of excess noise factor extraction methodology in the future work.

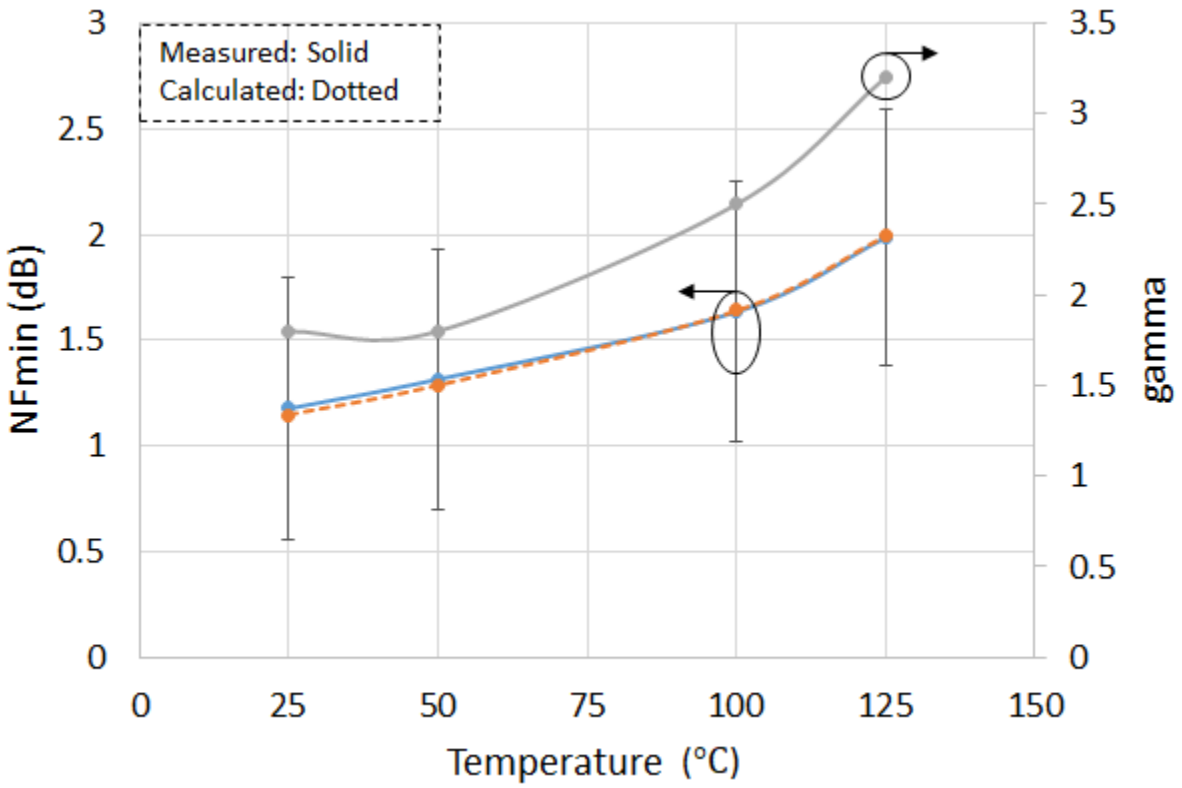

Figure 5.10. Sample 130 nm NMOS NF_{min} measured vs calculated with fitted excess noise factor γ at $V_{gs} = 1.2V$ and $V_{ds} = 1.2V$ at 10 GHz.

5.4 Conclusion

For RF CMOS devices, the origin and calculation methodology of excess noise factor are presented with the comparison of BSIM noise models. A good agreement of the noise parameters is obtained between the calculation and measurement. At the same time, this research calculated the excess noise factor based on the tuner-based noise measurement and S-parameter measurement and validated the high frequency noise model of MOSFET devices over bias with 130 nm and 40nm channel lengths.

CHAPTER 6

CONCLUSIONS AND FUTURE WORKS

6.1 Conclusions

This work has contributed to the overall understanding of the characterization and modeling of high frequency noise of BICMOS transistors. The noise transit time and noise ratio of SiGe HBT have been calculated from the HICUM model and shown to give a good agreement with the fitted values from the measurement. It was found that the noise transit time can be independent of frequency but dependent on temperature and biasing. The results indicate that the noise transit time and noise correlation effect can be well predicted from the HICUM compact model based on the parameter extraction methodology over the temperature and biasing.

In this work, the extraction of noise transit time from HICUM model has been discussed. Based on the transport noise model, the noise correlation effect of the high frequency noise of SiGe HBTs has been clarified.

The noise ratio is extracted from the calculation and validated over bias, temperature, size and technology scaling with sample SiGe HBTs.

For RF CMOS devices, the noise excess factor of NMOS has been calculated based on the Y-parameter noise calculation and tuner-based measurement. The Y-parameters noise calculation is derived based on the equivalent circuit.

The high frequency noise measurement is validated based on the device physics for both bipolar and NMOS devices.

6.2 Future Works

More works on investigating an experimental way (without the model) to more accurately determine the noise transit time can be considered in the future, since the extracted HICUM model parameters can introduce uncertainties in the noise transit time calculation. Therefore, a calculation method of noise transit time from the measured dc or S-parameters based on the device physics can be investigated in the future.

At the same time, investigating the origin of excess noise factor for short channel MOSFET can be a future direction. Since in sub-100-nm technologies, microscopic excess noise starts to play a significant role and its incorporation in thermal noise models is unavoidable. The excess noise factor can be effected by velocity saturation, channel length modulation and non-equilibrium effects for short channel MOSFETs. Therefore, to clarify the origin of excess noise based on the device physics can be considered as a research topic in the future.

REFERENCES

[1] J. S. Goo, “High Frequency Noise in CMOS Low Noise Amplifiers”, Ph. D. dissertation, The Department of Electrical Engineering, Stanford University, Aug, 2001.

[2] J. B. Johnson, “Thermal Agitation of Electricity in Conductors”, *Phys. Rev.* 32 (97): pp. 97-109, 1928.

[3] H. Nyquist, “Thermal Agitation of Electric Charge in Conductors”, *Phys. Rev.* 32 (110): pp. 110-113, 1928.

[4] Van der Ziel, “Theory of Shot Noise in Junction Diodes and Junction Transistors”, *Proc. IRE*, pp. 1639-1646, Nov. 1955.

[5] A. L. McWhorter, “1/f Noise and Germanium Surface Properties,” in *Semiconductor Surface Physics*. Philadelphia: University of Pennsylvania Press, 1957, p. 207.

[6] F. N. Hooge, “l/f noise,” *Physica*, vol. 83B, p. 14, 1976.

[7] H. T. Friis, “Noise Figure of Radio Receivers,” *Proceedings of the Insititude of Radio Engineers*, vol. 32, no. 7, pp 419-422, Jul. 1944.

[8] H. A. Haus et al., “Representation of Noise in Linear Two Ports” *Proceedings of the Insititude of Radio Engineers*, vol. 48, pp 69-74, Jan. 1960.

[9] K. H. K. Yau and S. P. Voinigescu, “Modeling and extraction of SiGe HBT noise parameters from measured Y-parameters and accounting for noise correlation,” in *Si Monolithic Integrated Circuits in RF Systems Dig.*, 2006, pp. 226–229.

[10] H. Hillbrand H. and P.H. Russer, “ An Efficient Method for Computer-Aided Noise Analysis of Linear Amplifier Networks”, *IEEE Trans. Circuit Syst.*, vol. CAS-23, pp 235-238, Apr 1976.

[11] C. H. Chen, “High Frequency Noise Modeling of MOSFETs”, Ph. D. dissertation, Simon Fraser University, Dec, 1997.

[12] G. Niu, “Noise in SiGe HBT RF technology: Physics, modeling and circuit implication,” *Proc. IEEE,* vol. 93, no. 9, pp. 1583–1597, Sep. 2005.

[13] P. Cheng and H. Shichijo, “High frequency noise characterization of BiCMOS transistors over temperature,” in *IEEE Dallas Circuits and Systems Conf. (DCAS),* Oct. 2016.

[14] K. Xia and G. Niu, “Discussions and extension of van Vliet’s noise model for high speed bipolar transistors,” *Solid-State Electronics,* vol. 53, pp. 349–354, Mar. 2009.

[15] R. L. Prichard, *Electrical Characteristics of Transistors*. New York, USA: McGraw-Hill Inc., pp. 234, 1967.

[16] J. te Winkel, “Extended Charge-Control Model for Bipolar Transistors”, *IEEE Trans. Electron Dev.,* Vol. ED-20, pp. 389-394, 1973.

[17] K. Xia and G. Niu, “Modeling the Input Non-quasi-static Effect in Small Signal Equivalent Circuit Based on Charge Partitioning for Bipolar Transistors and Its Impact on RF Noise Modeling,” *Solid-State Electronics,* vol. 54, pp. 1566–1571, Dec. 2010.

[18] S. Decker, B. Heinemann, C. Jungemann, B. Meinerzhagen and B. Neinhus, “Investigation of high frequency noise in a SiGe HBT based on Shockley’s impedance field method and hydrodynamic model,” in *Technical Proc. International Conf. Modeling and Simulation of Mecrosystems,* 2000, pp. 364–367.

[19] Z. Xu, G. Niu, and R. M. Malladi, “Compact modeling of collector base junction space charge region time effect on noise in SiGe HBTs,” in *Proc. IEEE Silicon Monolithlic Integr. Circuits RF System (SiRF*), 2010, pp. 180–183.

[20] H. Y. Chen, et al. “Small-Signal Modeling of SiGe HBTs Using Direct Parameter-Extraction Method,” *IEEE Transaction on Electron Devices*, vol. 53, No. 9, Sep, 2006.

[21] U. Basaran, N. Wieser, G. Feiler, and M. Berroth, “Small-signal and high-frequency noise modeling of SiGe HBTs,” *IEEE Trans. Microw. Theory Techn.*, vol. 53, no. 3, pp. 919–928, Mar. 2005.

[22] J. Herricht et al., “Systematic compact modeling of correlated noise in bipolar transistors”, *IEEE Trans. Microw. Theory Techn.*, vol. 60, no. 11, pp. 3403–3412, Nov. 2012.

[23] B. Banerjee, S. Venkataraman, C.-H. Lee, and J. Laska, “Broadband noise modeling of SiGe HBT under cryogenic temperatures,” in *IEEE Radio Freq. Integr. Circuits (RFIC) Symp.*, 2007, pp. 765–768.

[24] B. Li and S. Prasad, “Basic expressions and approximations in small-signal parameter extraction for HBT’s,” *IEEE Trans. Microw. Theory Techn.*, vol. 47, no. 5, pp. 534–539, May. 1999.

[25] M. Schröter and A. Chakravorty, *Compact Hierarchical Bipolar Transistor Modeling with HICUM.* Singapore: World Scientific, 2010.

[26] M. Schröter and T. Y. Lee, “Physics-based minority charge and transit time modeling for bipolar transistors,” *IEEE Trans. Electron Devices*, vol. 46, no. 2, pp. 288–300, Feb. 1999.

[27] P. Cheng and H. Shichijo, “Prediction of noise transit time and noise correlation of SiGe HBTs”, in *Proc. IEEE Silicon Monolithlic Integr. Circuits RF System (SiRF*), 2018, pp. 64–67.

[28] P. Cheng and H. Shichijo, “High frequency noise characterization and modeling of SiGe HBTs”, in *IEEE Trans. Microw. Theory Techn.*, vol. 66, no. 12, pp. 5169–5175, Oct. 2018.

[29] S. J. Spiegel, D. Ritter, R. A. Hamm, A. Feygenson, and P. R. Smith, “Extraction of the InP/GaInAs heterojunction bipolar transistor small-signal equivalent circuit,” *IEEE Trans. Electron Devices*, vol. ED-42, pp. 1059–1064, June 1995.

[30] J. Krause and M. Schröter., “Methods for determining the emitter resistance in SiGe HBTs: A review and an evaluation across technology generations*”, IEEE Trans. Electron Devices*, vol. 62, no. 5, pp. 1363–1374, May 2015

[31] F. Stein, Z. Huszka, N. Derrier, C. Maneux, D. Celi, “Extraction Procedure for Emitter Series Resistance Contributions in SiGeC BiCMOS Technologies,” in *2014 IEEE Conference on Microelectronic Test Structures*, Mar 2014.

[32] T. Nakadai and K. Hashimoto, “Measuring the base resistance of bipolar transistors,” in *Proc. BCTM*, 1991, pp. 200–203.

[33] A. Pawlak, J. Krause, H. Wittkopf, and M. Schröter, “Single transistor based methods for determining the base resistance in SiGe HBTs: Review and evaluation across different technologies,” *IEEE Trans. Electron Devices*, vol. 63, no. 12, pp. 4591–4602, Dec. 2016.

[34] M. Schroter, S. Lehmann, ‘’The rectangular bipolar transistor tetrode structure and its application,” *IEEE International Conference on Microelectronic Test Structures*, March 2007.

[35] Harame, et al., “Si/SiGe Epitaxial-Base Transistors”, *IEEE Trans. Electron Devices*, vol. 42, no. 3, pp. 455–482, Mar. 1995.

[36] A. Van der Ziel, Solid State Physical Electronics, Chapter 18, Prentice-Hall,Englewood Cliffs, NJ, 3rd Edition, 1976.

[37] G. J. J. Smit, et al., “RF-noise modeling in advanced CMOS technologies.” *IEEE Transaction on Electron Devices 2014*, pp. 245-254.

[38] BSIM 4.80 Model Manual, University of California, Berkeley.

[39] S. H. Jen, et al., “Accurate Modeling and Parameter Extraction for MOS Transistors Valid up to 10 GHz.” *IEEE Transaction on Electron Devices*, Nov 1999.

BIOGRAPHICAL SKETCH

Peng Cheng was born in Daqing, China, in 1991. He has been an IEEE Student Member since 2018. He received a BS degree in Electrical Engineering from Harbin Engineering University, Harbin, Heilongjiang, China, in 2013. He received his MS degree in Electrical Engineering from The University of Texas at Dallas, Richardson, TX, USA, in 2015. He is currently working toward a PhD degree on RF device characterization and modeling at The University of Texas at Dallas.

In Aug. 2017, he served an internship at Texas Instruments. In July 2018, he served an internship at Skyworks Solutions Inc. He is currently a Research Assistant with the Department of Electrical and Computer Engineering, University of Texas at Dallas.

CURRICULUM VITAE

Peng Cheng

August 17, 2019

Contact Information:

Department of Electrical Engineering
The University of Texas at Dallas
800 W. Campbell Rd.
Richardson, TX 75080-3021, U.S.A.

Email: solo.chengpeng@gmail.com

Educational History:

B.S., Electrical Engineering, Harbin Engineering University, 2013
M.S., Electrical Engineering, The University of Texas at Dallas, 2015
Ph.D., Electrical Engineering, The University of Texas at Dallas, 2019

Employment History:

Teaching/Research Assistant, The University of Texas at Dallas, September 2014 – present
RF SOI Switch Design Co-Op, Skyworks Solutions Inc., July 2018 – December 2018
RF Development Engineer Intern, Texas Instruments, August 2017 – December 2017

Professional Memberships:

Institute of Electrical and Electronics Engineers (IEEE)

Publications:

[1] P. Cheng and H. Shichijo, "High frequency noise characterization and modeling of SiGe HBTs", in *IEEE Trans. Microw. Theory Techn.*, vol. 66, no. 12, pp. 5169–5175, Oct. 2018.

[2] P. Cheng and H. Shichijo, "Prediction of noise transit time and noise correlation of SiGe HBTs", in *Proc. IEEE Silicon Monolithlic Integr. Circuits RF System (SiRF*), 2018, pp. 64–67.

[3] P. Cheng and H. Shichijo, "High frequency noise characterization of BiCMOS transistors over temperature", in *IEEE Dallas Circuits and Systems Conf. (DCAS)*, Oct. 2016.

[4] P. Cheng and H. Shichijo, "High Frequency Noise Characterization of BiCMOS Transistors over Temperature", poster presentation at TECHCON 2016, Sep. 2016.